RNA Targets and Function of Topoisomerase 3β in Reducing Stress in Neuronal Physiology

Shohreh Teimuri, Masaba Baroi Sayor, and Beat Suter*

Institute of Cell Biology, University of Bern, Berne, 3012, Switzerland

*Corresponding address: Beat.Suter@unibe.ch

Abstract

Topoisomerase 3β (Top3β) relaxes DNA and RNA and its dysregulation is implicated in various neurodevelopmental and cognitive disorders. We developed a novel protocol to isolate RNA targets of the topoisomerase without artificial cross-linking and demonstrated that topoisomerase activity toward long RNAs is useful in cells where mRNAs travel over long distances and require strict translational control. We show that such mRNAs depend on the RNA topoisomerase activity for their proper expression and localization. Lack of the enzymatic activity of Top3β stresses neurons, affecting the morphology of the neuromuscular junction (NMJ) in larvae and adult flies, aging, and the coordinated movement of older flies. The interaction network of Top3β links it to all levels of posttranscriptional RNA expression, splicing, localization, translation, and RNA stability. This study provides insights into the mechanisms underlying neurological diseases, including schizophrenia, autism spectrum disorders, and Fragile X syndrome, diseases to which Top3β and many of its interactors, particularly Tdrd3 and FMR1, have been linked.

Introduction

Topoisomerase 3β (Top3β) is an RNA-binding protein (RBP) with dual enzymatic activity toward DNA and RNA (1). Topoisomerases are better known for their activity toward DNA, where they resolve tension and supercoiling. Much less is known about the function of topoisomerases toward RNA. Along with other RBPs, Top3β contributes to mRNA translation, particularly in the nervous system, which is significant for neurodevelopment and psychological and physical well-being (2). Its functional importance is suggested by results that link impaired *Top3β* function to various neurodevelopmental and cognitive disorders (2)(3).

Drosophila melanogaster Top3β possesses the key feature of a topoisomerase. The predicted catalytic tyrosine residue is present at position 332 (Y332) and is essential for its topoisomerase activity (4). Top3β topoisomerases distinguish themselves from other topoisomerases by their conserved RNA-binding motif called RGG (Arginine Glycine Glycine) box, which binds to RNAs or proteins. Its paralogue Top3α, a DNA topoisomerase, possesses the catalytic tyrosine residue but lacks the RGG box (4). *In vitro*, the RGG box is not required for the enzymatic activity but might play a role in binding to the RNA and thereby facilitate the enzymatic activity *in vivo* (2).

We hypothesized that the neurological requirements for a topoisomerase, which acts on RNAs, might reflect, in part, its activity on mRNAs that need to be transported over long distances to be translated at the right time at the right place. During such transport, long linear molecules, such as mRNAs, are likely to become entangled or suffer other structural problems that might interfere with their transport, (un)packaging, and translation (1). A topoisomerase that acts on RNA might, therefore, be able to rescue such RNAs. Particularly in large cells, where mRNAs need to travel over long distances, a topoisomerase could provide an important advantage and allow the cell to function properly. Drosophila has such large cells in the nervous system, the female germline, and the young, syncytial embryo. We, therefore, set out to study the activity and function of Drosophila Top3β in the young embryo and the nervous system to identify relevant *in vivo* RNA targets, interacting proteins, and biological functions.

57 Consistent with the notion that larger RNAs are more likely to encounter structural problems
58 in living cells, we found that longer RNAs are more likely to be targets of Top3β in young
59 embryos. Comparing the phenotype caused by the specific mutations (Y332F and ΔRGG) with
60 the null phenotype tells us whether the enzymatic activity or RNA and protein binding are
61 important for the normal function of Top3β in the affected process. Specifically, we wanted
62 to test the involvement of these elements in localizing the identified Top3β RNA targets and
63 facilitating the local accumulation of the encoded proteins. Here we show that this is the case
64 and that Top3β is needed for the normal accumulation of localized proteins encoded by
65 mRNAs that are targets of Top3β. Accordingly, the lack of this enzyme stresses the affected
66 tissue and causes signs of neurodegeneration and premature aging.

67 ## Results

68 Drosophila *Top3β* is preferentially expressed in the female germ line as part of the maternal
69 contribution deposited in the egg to support embryogenesis. *Top3β* is also expressed at high
70 levels in the nervous system. We, therefore, wanted to find out how important Top3β is in
71 these tissues and stages for proper development and physiological function and whether it
72 contributes to RNA localization and controlled local translation in these large cells and cells
73 with long extensions.

74 **RNA interactions of Top3β in embryos and heads**

75 To identify the RNA targets to which Top3β binds and performs its topoisomerase activity, we
76 sequenced the RNAs isolated by immunoprecipitation (IP). This was done using animals that
77 expressed an eGFP fused to wild-type Top3β, Top3β in which Y332 was replaced by a
78 phenylalanine (Y332F), and Top3β with the RGG box deleted (ΔRGG). An eGFP-expressing line
79 served as an additional negative control.

80 During its enzymatic reaction, Top3β forms a covalent bond between its Y332 side chain and
81 the RNA targets (5). Using this to our advantage, we added an ionic detergent at low
82 concentration to the IP, conditions that should pull down primarily covalently bound RNAs
83 without denaturing the antibodies and their interactions. The covalent bond between Top3β's
84 Y332 and the RNA targets was stabilized for the IP by removing Mg^{2+}, which is needed for the
85 enzyme to resolve the bond at the end of the enzymatic reaction (6). To determine if the
86 target RNAs were specifically bound to the –OH group of Y332, we used the Y332F mutant as
87 a negative control, as it does not have this -OH group and, therefore, cannot form the covalent
88 bond. The RNAs that are enriched in the wild type compared to the Y332F mutant can be
89 considered to be targets of the catalytic activity of Top3β **(Supplementary Table S1, S2)**.

90 The candidate RNA targets that depend on Y332 with adjusted p-value (adjp-value) <0.05 and
91 log2FC>1 were selected and ranked based on their adjp-value. We used 46 embryonic RNA
92 targets and the top 50 head RNA targets for further analyses (**Supplementary Table S3, S4**).
93 Because long RNAs seem more likely to depend on this enzymatic activity, we further tested
94 the quality of the data by comparing the RNA length of the presumed targets with the
95 background RNA length and found that in embryos, longer RNAs were more likely to
96 covalently bind to Top3β as they showed higher enrichment in the wild-type extracts

97 compared to the *Top3β*^{Y332F} mutant extracts (**Fig. 1A; Supplementary Table S1, S2**). The
98 results might also reflect that longer RNAs have a higher chance of enduring physical stress
99 and are therefore also for this reason more likely to become substrates of the enzymatic
100 activity of Top3β. In the head extracts, this was not the case (**Fig. 1B**). It is not clear whether
101 this is due to the much higher cellular diversity in the head, the smaller cell sizes compared
102 to the syncytial embryos, or another reason.

103 We next analyzed which RNA features correlate with the chance of becoming a target of
104 Top3β's enzymatic activity. The results showed that embryonic Top3β targets had on average
105 longer 3'UTRs and stemmed from larger genes with longer introns compared to the complete
106 set of different types of RNAs detected in the wild-type RNA-IP (**Fig. 1C-D, Supplementary**
107 **Table S1, S2)**. Both embryonic and head Top3β targets had a higher number of transcript
108 isoforms per gene and more exons (**Fig. 1E-F, Supplementary Table S1, S2)**.

109 A compartment enrichment analysis revealed that the encoded proteins of the top 50 head
110 RNA-IP targets were predominantly located in the plasma membrane, the cortex, and in
111 mitochondria. Mutants in the corresponding top 50 head genes are mainly enriched for
112 neurophysiology phenotypes in *Drosophila,* whereas the genes for the embryonic RNA-IP
113 targets had been associated with several phenotypes in Drosophila, including abnormal
114 neurophysiology.

115 **Homologs of Drosophila Top3β target mRNAs bind also mammalian Top3β and FMRP1**

116 Comparing our Top3β RNA-IP results with those obtained from the shared targets of FMRP1
117 (HITS-CLIP data of FMRP produced from mouse brain extracts) and Top3β (HITS-CLIP data of
118 Flag-Top3β from HeLa cells; (1)) revealed intriguing similarities. A Venn diagram illustrates the
119 overlap between the top targets of Drosophila Top3β and the shared mammalian targets,
120 with the number of such overlapping targets listed in **Fig. 2**. The common feature of the
121 proteins encoded by the shared RNA targets is that they are predominantly large proteins.
122 Many are localized to the plasma membrane or the cell cortex (e.g., Sev, Mgl, α-Spec, Kst,
123 Pcx) or cytoskeleton-associated (e.g., Dhc64C, Mhc, Myo10A, α-Spec, Kst), have axonal
124 functions (e.g., Shot, Dhc64C, Kst, Prosap), or scaffolding functions (Shot, Prosap).

125

Figure 1:

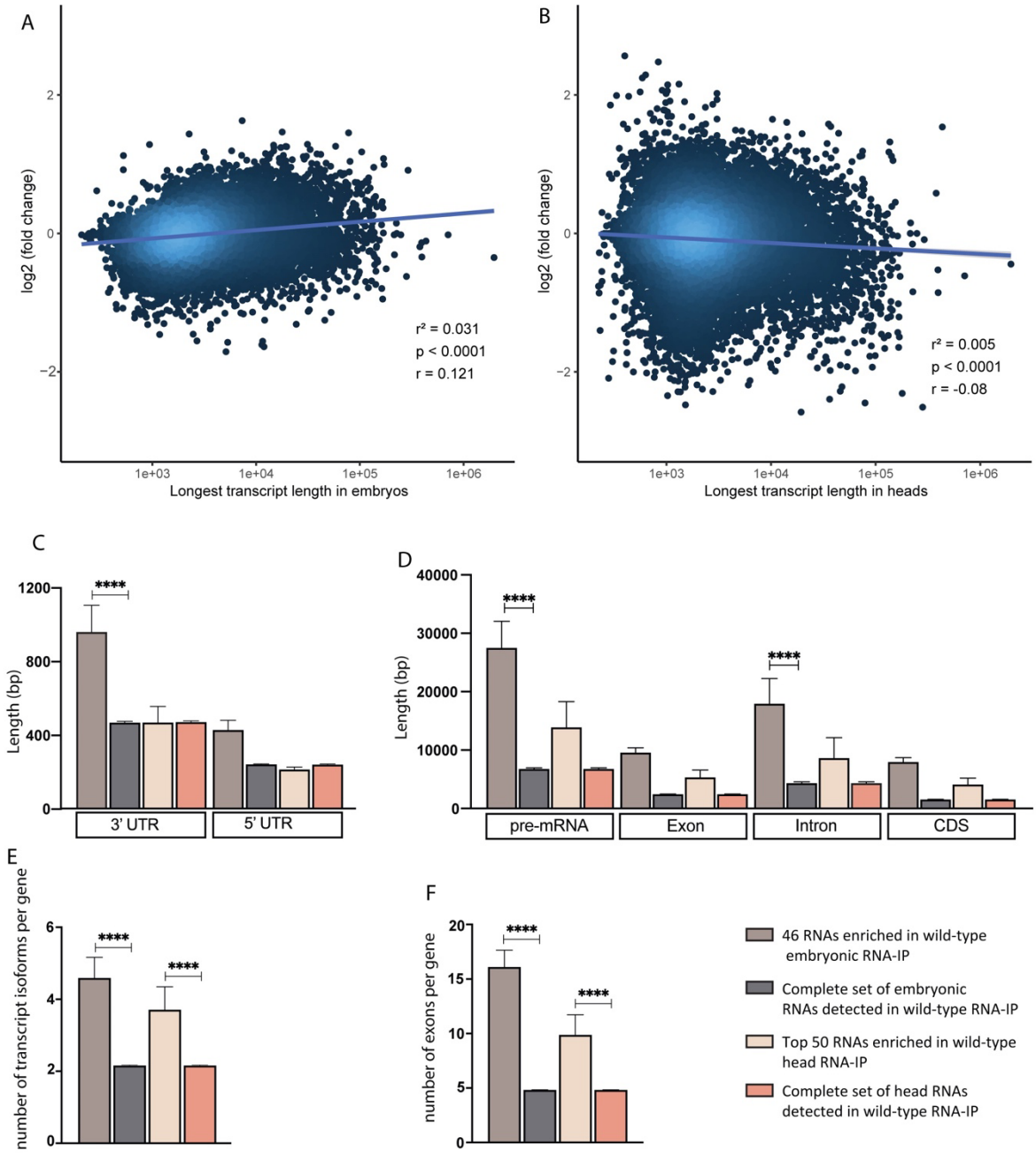

Fig. 1. RNA features of enzymatic targets of Top3β. Extracts were from A) embryos and B) heads. A) Longer RNAs are more likely targets of the enzymatic activity of Top3β because they are more enriched in the IP with the wild-type Top3β compared to the Top3β^{Y332F}. B) No correlation between the length of the bound RNAs and their covalent binding to Top3β was observed in head extracts. r measures the strength of the correlation and p stands for p-value. C-F) Transcript features for the embryonic RNA targets (46 RNAs) and the top 50 head RNA targets of Top3β sorted according to the adjp-value. The complete sets of RNAs detected in the wild-type RNA-IP served as the standard. p-value <0.0001=****, p-value <0.001=***, p-value <0.01=**, p-value <0.05=*

Figure 2:

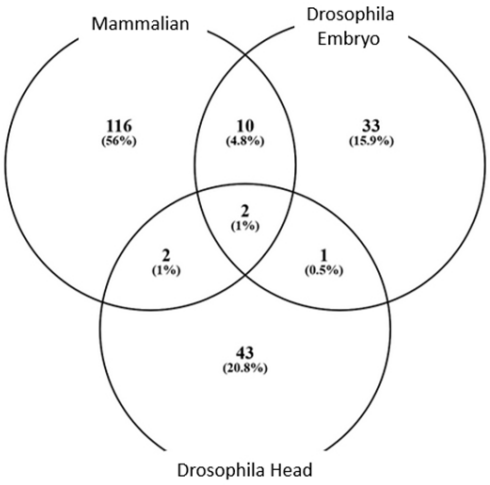

Homologous targets in "mammalian", "Drosophila embryo" and "Drosophila head"	Homologous targets in "mammalian", and "Drosophila head"	Homologous targets in "mammalian", and "Drosophila embryo"	
Sev Myo10A	Mhc mgl	Pcx Shot Bruce FASN1 HERC2	Kst α-Spec Dhc64C Prosap Smr

Fig. 2. Homologous targets shared between Drosophila Top3β and mammalian FMRP1 and Top3β. Venn diagram for the RNAs shared between our study (Drosophila head and embryo RNA-IPs) with the previous mammalian study (1), which revealed the overlap of the interactors with mouse FMRP1 from brain extracts and Top3β interactors in HeLa cells. The list of the Drosophila homologs that were also found in both mammalian interactor screens is also shown.

126 **The interaction network of RNA Top3β**

127 To identify factors that might contribute to the Top3β activity, immunoprecipitations (IP) on
128 extracts from 0-2 hours old embryos and 1-5 days old heads were performed using the same
129 three alleles of *Top3β-eGFP* and the *eGFP* control line. The proteins present in the IP
130 complexes were analyzed using mass spectrometry (MS) and their abundance was compared
131 to the eGFP control. Proteins with an adjusted p-value <0.01 and log2FC >1 were retained
132 from the analysis of the wild-type Top3β::eGFP/eGFP embryo IPs and this resulted in 426
133 proteins. Proteins with an adjusted p-value <0.05 and log2FC >1 were retained from the
134 analysis of the wild-type Top3β::eGFP/eGFP head IPs and this yielded 67 proteins
135 (**Supplementary Table S5, S6).**

136 Ribosomal proteins were particularly highly represented among the IP interactors. 89 in the
137 set of embryonic interactors and ten among the head interactors. After excluding ribosomal
138 proteins from this list, a gene ontology enrichment analysis on the top 100 (according to
139 log2FC) embryonic proteins **(Fig. 3A)** and the remaining 57 head proteins **(Fig. 3B)** was
140 performed. Particularly the analysis of the embryonic data revealed enrichment for proteins
141 involved in the activation of translation, P-bodies, stress granules, and neural
142 ribonucleoprotein granules, all membrane-less structures involved in storing specific mRNAs
143 during periods of stress or concentrating mRNAs and regulatory proteins (7). Additionally, the
144 interactors were also enriched in several functions related to mitochondria.

145 Pointing to high conservation of the activity of Top3β between the two very different stages
146 and tissues, 17 of the 57 non-ribosomal head proteins were also identified as interactors in
147 the embryonic IPs and 8 of the 10 ribosomal head proteins were also identified as interactors
148 in the embryonic IPs **(Fig. 3C; Supplementary Table S5, S6).**

149 **Proteins that require Tyr332 (Y332) or the RGG box for binding**

150 Tdrd3, a well-known interactor of Top3β (8), was among the top enriched proteins in both
151 embryonic and head IPs, suggesting that our immunoprecipitation was specific. To assess the
152 role of the Y332 residue and the RGG box in Top3β interactions, we compared the IP results
153 with the ones from the *Top3β* mutants *Top3β*^{Y332F} and *Top3β*$^{\Delta RGG}$. Among the 337 non-
154 ribosomal binding candidates in the embryos, 102 proteins needed the Y residue and the RGG
155 box to bind to Top3β because they were not enriched in the protein-IP from either mutant

Figure 3:

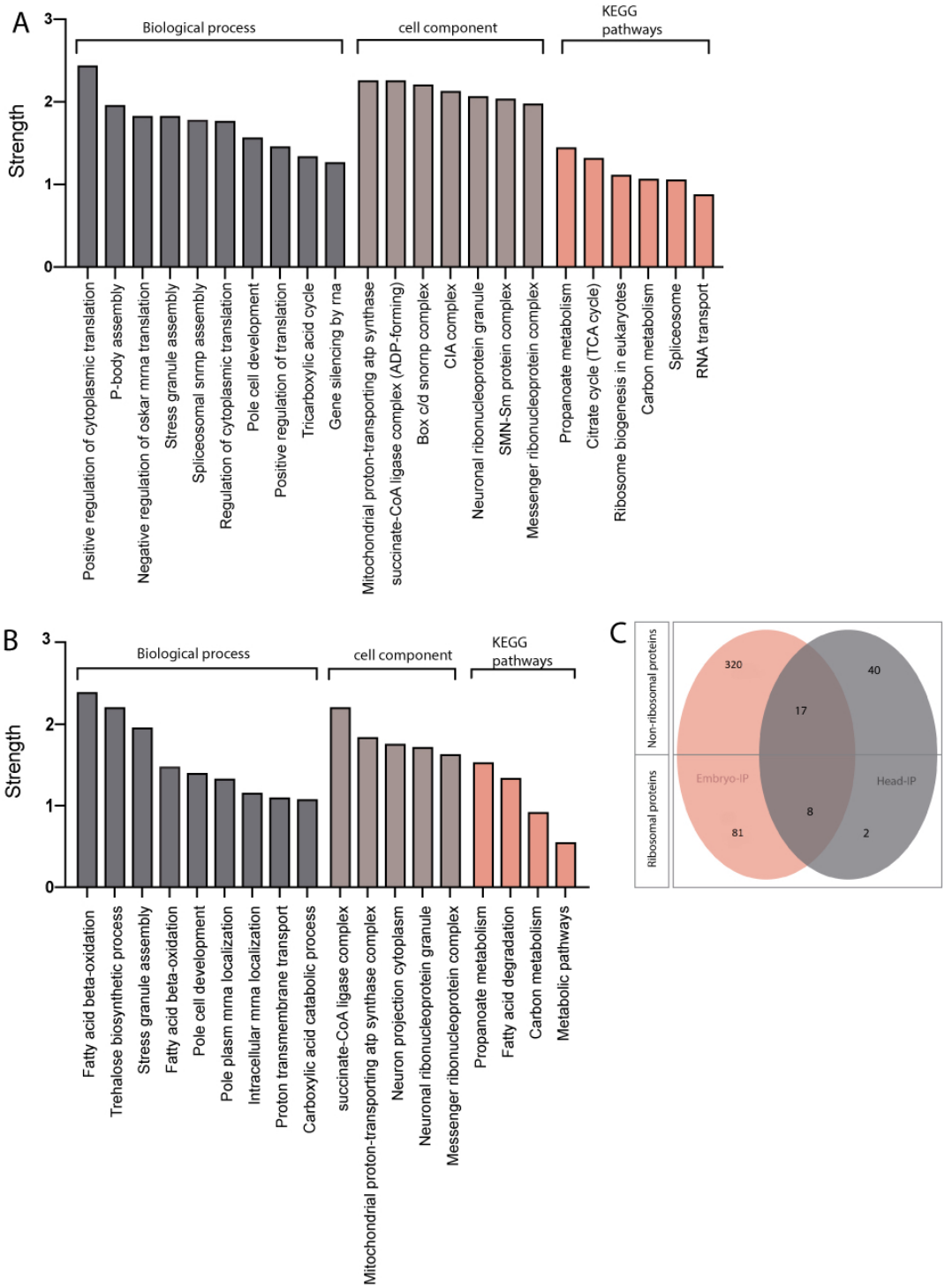

Fig. 3. Gene ontology enrichment for Top3β-associated proteins. A) Gene ontology enrichment for Top3β-associated proteins for the top 100 interactors from embryonic extracts and B) Gene ontology enrichment for Top3β associated proteins for 57 head interactors. Strength shows the Log10 of the enrichment according to StringDB (80). C) Number of proteins that were common in the head and embryo protein-IP.

156 **(Supplementary Table S5, S6)**. An additional 16 proteins needed Tyr (but not RGG) for their
157 binding and 23 proteins were dependent on the RGG box (but not on Y332F) for their binding
158 to Top3β. In the data set from heads, of the 57 non-ribosomal binding proteins, 2 proteins
159 were not enriched in the Y332F mutant, 33 were not enriched in the ΔRGG mutant, and no
160 protein was absent from both mutant IPs. Proteins absent only from one of the two mutants
161 are likely to bind either directly to the corresponding site in the wild-type Top3β or interact
162 with an RNA or protein that binds to it.

163 The analysis of the IP results revealed that more proteins required the RGG box to interact
164 with Top3β, and these proteins are involved in RNA transport, splicing, mRNA surveillance,
165 and degradation processes. In contrast, proteins that required the Y332 residue were only
166 involved in RNA transport or splicing based on the KEGG pathway analysis. In addition, a visual
167 inspection of the interaction map (described in the next paragraph) also revealed many
168 translation factors among the Y332-dependent interactors **(Fig. 4A)**. The large difference in
169 the numbers of interacting proteins between embryo and head protein-IPs was striking. These
170 differences were seen for the binding to the RGG and Y332 motives.

171 A physical interaction map of the proteins enriched in the Top3β::GFP IP was created using
172 Cytoscape-String. In this way, the first, second, and subsequent interactors of Top3β were
173 determined (**Fig. 4)**. Entering the results from the mutant analyses into this map gave an idea
174 at which level the different proteins might interact with Top3β and which other proteins they
175 might need for their interaction. The map derived from the embryonic protein IPs resolves
176 two distinct processes (**Fig. 4A)**. The right branch is enriched in cytoplasmic proteins and
177 includes Tdrd3, FMR1, the piRNA pathway, and translation. The left branch connects Top3β
178 functions to its nuclear functions and includes the splicing activity. Many proteins identified
179 by the head protein-IPs are shared with the embryo protein-IP set, particularly in the
180 cytoplasmic branch (**Fig. 4B)**.

181 Me31B was identified as an interactor in both embryonic and head protein-IPs and its
182 interaction with Top3β turned out to be dependent on the RGG box in the embryonic protein-
183 IPs. Me31B is an ATP-dependent RNA helicase and a core component of a variety of
184 ribonucleoprotein complexes (RNPs) that play critical roles in translational repression and
185 mRNA decapping during embryogenesis, oogenesis, neurogenesis, and neurotransmission
186 (9)(10)(11)(12)(13)(14)(15)(16). Me31B is part of an RNP complex containing Tral, eIF4E1,

Figure 4

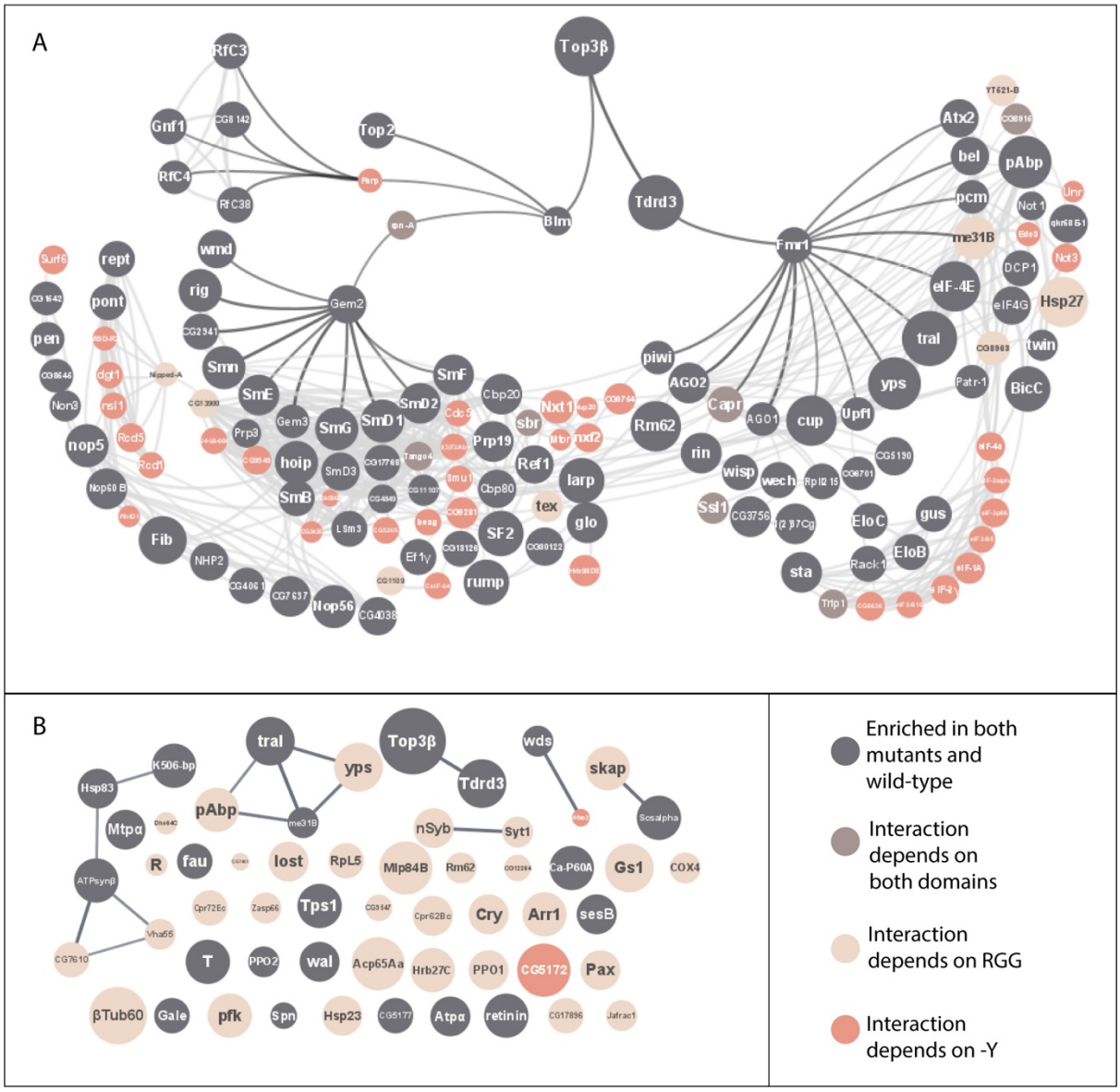

Fig. 4. Protein-IP physical interaction. A) proteins enriched in the embryo protein-IP with their physical interactions. Proteins that ended up further away from Top3β than the ones shown here, were removed from the interaction map. B) Proteins enriched in the head protein-IP with their physical interactions. The size of the bulbs represents the enrichment in the protein-IP. The color of the bulbs indicates whether their interactions with Top3β depend on Y332 or the RGG box.

187 Cup, and pAbp, that is involved in RNA localization and RNP-mediated translational repression
188 of maternal mRNAs during oogenesis and embryogenesis (13). Me31B is located relatively
189 close to Top3β in the physical interaction map and the other complex proteins, Tral, eIF4E1,
190 Cup, and pAbp, were enriched in the embryonic protein-IP.

191 **Biological relevance of Top3β activity**

192 The *Top3β*^{Y332F} and *Top3β*^{26} mutants have reduced or no function, but the mutations neither
193 cause lethality nor sterility. This is a common phenomenon observed with genes and proteins
194 that are still important for optimizing cellular physiology in the wild. In a lab setting, the
195 reduced function of these mutants can often be compensated for by other mechanisms.
196 However, by directly analyzing the cellular phenotypes of the mutants, one may observe
197 increased cellular stress and changes in physiology or anatomy that reveal the cellular
198 function of the normal gene. Such cellular stress and changes often lead to signs of premature
199 aging, like a decline in neuromuscular performance and a shorter lifespan.

200 ***Role of Top3β for localizing and expressing its transcript targets***

201 To evaluate the consequences of the interaction of Top3β with its RNA targets, we selected 5
202 genes (*shot*, *Pfrx*, *Hers*, *Dhc64C*, and *kst)* from the embryo RNA IP top list for further analysis.
203 These RNAs exhibit several distinctive features, including a high number of transcript
204 isoforms, long mRNAs, localized mRNAs, and maternal expression. *shot*, *Dhc64C*, and *kst* were
205 also on the list of our shared targets with the previous mammalian study (Fig. 2; (1)) and they
206 are also expressed in neurons (17)(18). We first assessed the effect of *Top3β* mutants on the
207 expression and subcellular localization of the *shot* mRNA in young embryos. The embryos
208 analyzed were maternally and zygotically either wild type or mutant. In the wild type, *shot*
209 mRNA accumulates more strongly in the polar granules and the pole cells at the posterior end
210 (**Fig. 5)**. This expression depends on *Top3β* and particularly on its enzymatic activity because
211 *shot* mRNA levels are reduced and the more intense localization pattern in the posterior pole
212 region is lost in the null- and the *Top3β*^{Y332F} mutant, but not in *Top3β*$^{\Delta RGG}$.

213 To investigate the effect of Top3β on the expression and subcellular localization of the
214 proteins encoded by the selected *Top3β* target RNAs, we also stained wild-type and mutant
215 embryos for these proteins. The resulting Shot signal was weaker in the entire null mutant
216 and *Top3β*^{Y332F} embryos compared to the wild type. Given that the mRNA levels were also

Figure 5:

(a version of Fig. 5 with better resolution and contrast is appended)

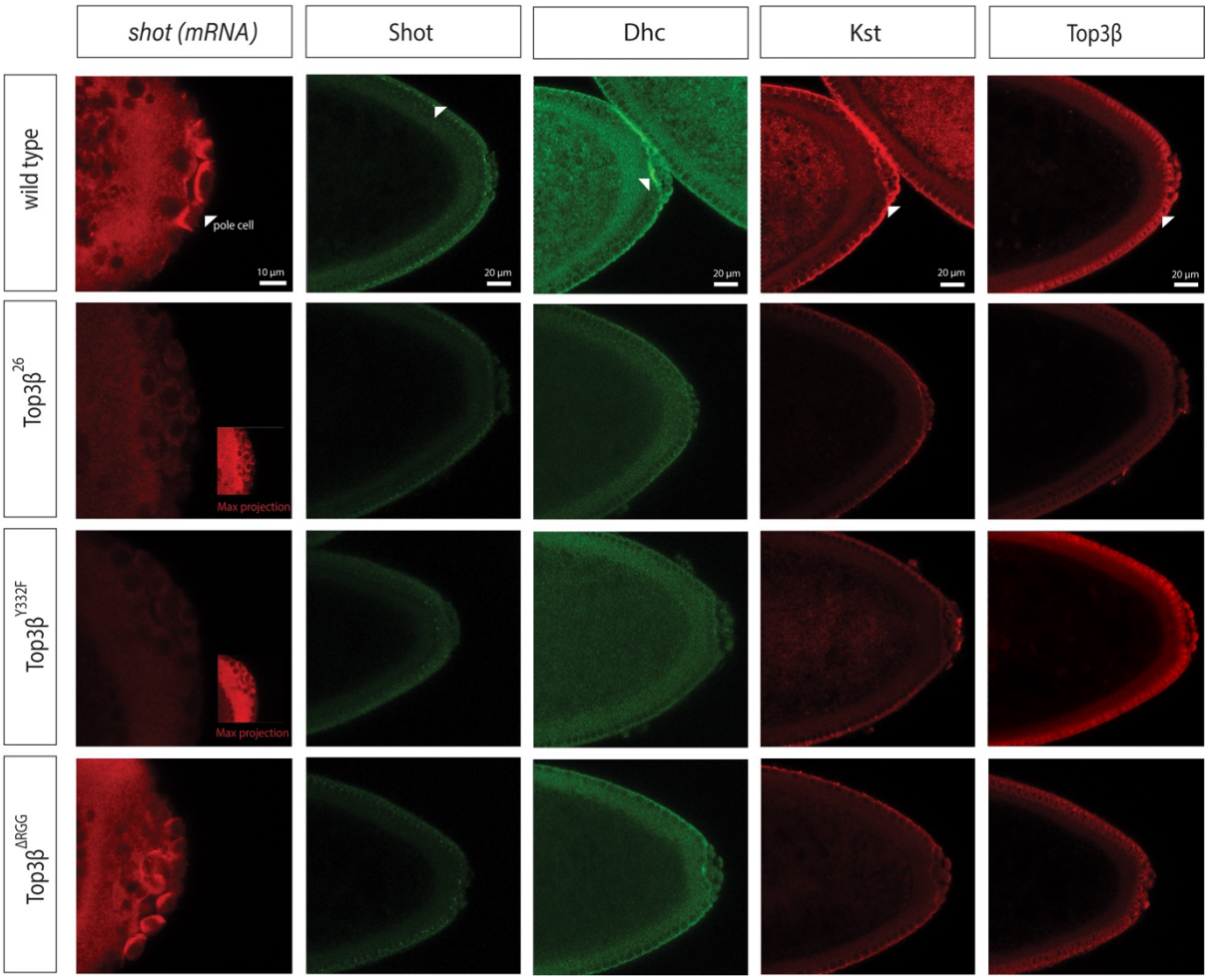

Fig. 5. Expression and localization of RNA targets and their encoded proteins. The posterior pole of the embryos is shown to the right. *shot* mRNA and Shot protein localization in the posterior part of syncytial (*shot* mRNA) and cellularizing (Shot protein) wild-type embryos and the different *Top3β* mutants. Lower signal levels and less localized signals were seen in the null and *Top3β*^{Y332F}. Both were less reduced in *Top3β*$^{\Delta RGG}$ mutant embryos. Note the *shot* mRNA localization in the pole cells in the wild type and *Top3β*$^{\Delta RGG}$ mutant. Dhc64C localization at the posterior side of the somatic part of the embryo (arrowhead) was not detectable in null mutants and *Top3β*^{Y332F} and reduced in the *Top3β*$^{\Delta RGG}$ mutant embryo. Kst localization at the apical membrane (arrowhead) was reduced in the null mutants and *Top3β*^{Y332F} compared to the wild type. Its localization was still identifiable in the *Top3β*$^{\Delta RGG}$ mutant embryo. Top3β protein is localized similarly to its targets. It is, however absent from the null mutant which reveals the background level of the staining. Note also that Top3β is also nuclear in the wild type and *Top3β*^{Y332F}. Imaging settings were identical for the staining for the same protein or mRNA in the different genotypes except for the insets which are overexposed to reveal the embryo. The scale bar is 10µm for the *shot* mRNA pictures and 20µm for the other micrographs.

217 reduced in similar ways, this decreased protein level could result from reduced RNA synthesis
218 or processing (splicing), or from RNA instability. These findings are consistent with *shot* mRNA
219 being the primary target of Top3β and they highlight the importance of the enzymatic activity
220 of Top3β for the efficient expression and localization of the encoded protein. In the *Top3β*$^{\Delta RGG}$
221 mutant embryos, the Shot protein levels and localization were also less affected, as the mRNA
222 levels were **(Fig. 5)**.

223 The Dynein heavy chain (Dhc or Dhc64C) protein accumulates more strongly at the posterior
224 end of the wild-type embryo, in front of the pole cells. This was neither detectable in the null
225 mutant nor in *Top3β*^{Y332F} **(Fig. 5)**. The Kst protein accumulates at the apical cortex in normal
226 blastoderm embryos, but in the *Top3β* null mutant and *Top3β*^{Y332F} its signal was reduced
227 throughout the embryo, including the apical cortex. It is conceivable that this decreased
228 protein abundance results from reduced RNA synthesis (e.g., splicing) or stability, or a
229 reduced translation of the mRNA. Protein signals for Dhc and Kst showed an intermediate
230 level in the *Top3β*$^{\Delta RGG}$ mutant embryos **(Fig. 5)**, indicating that the RGG box also affects their
231 expression, but less than the catalytic activity.

232 Top3β normally localizes to the same area in the blastoderm embryo where the different
233 proteins and mRNAs described here localize. We note that the wild-type protein and
234 Top3β^{Y332F} localize to the cytoplasm and the nuclei **(Fig 5)**. In contrast, Top3β$^{\Delta RGG}$ is clearly
235 seen above the background only in the cytoplasm. This indicates that its RGG box is needed
236 to move Top3β from the cytoplasm to the nucleus and that the lack of the RGG box likely
237 reduces the nuclear functions of Top3β$^{\Delta RGG}$.

238 ***Top3β affects the NMJ morphology in larvae and adults***

239 Larval motoneurons have been studied extensively to reveal developmental and physiological
240 effects on synapse morphology and function. We quantitatively compared the morphology of
241 the L3 larval NMJs on muscle 4 of the abdominal hemisegments 3, 4, and 5 between the wild
242 type and the three mutant *Top3β* alleles using *Drosophila_NMJ_morphometrics* (19) **(Fig. 6;**
243 **Supplementary Fig. S1)**. In most cases, the alleles revealed an allelic series where the
244 phenotypes were stronger in the null mutant, followed by the *Top3β*^{Y332F} and the *Top3β*$^{\Delta RGG}$
245 mutant. The number of boutons, active zones, and areas was significantly higher in the null
246 mutant (**Figs. 6A-C; Fig. 7)**. Aside from revealing a role in the normal establishment of NMJs,

Figure 6:

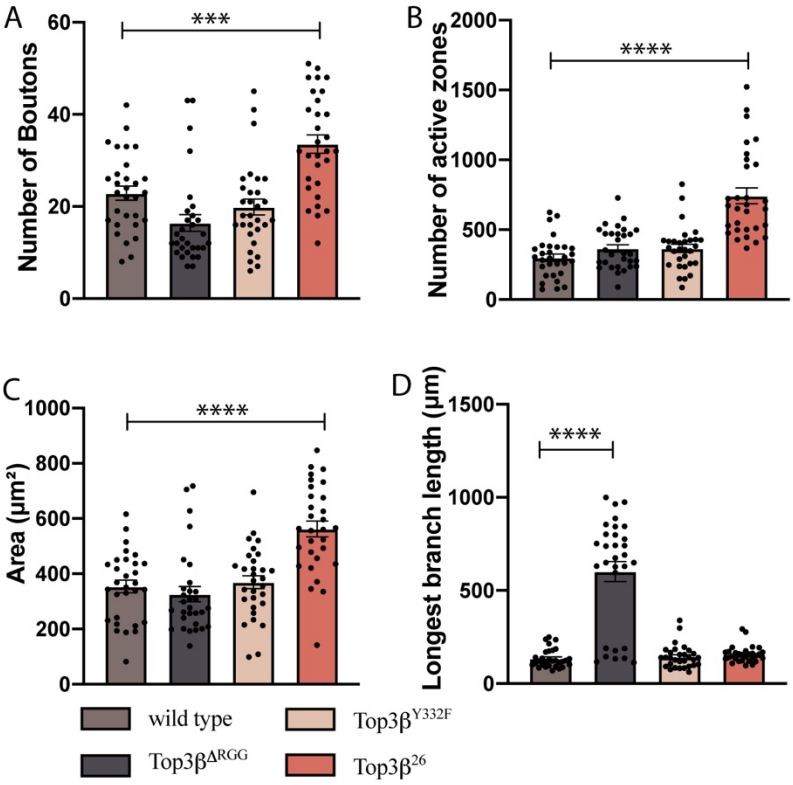

Fig. 6. NMJ morphometrics. Quantification of synaptic morphogenesis from NMJ4 abdominal segments A3-A5 of both sides of third instar wandering larvae (n=30, both males and females). The graphs are scatterplots and error bars represent the standard error of the mean (S.E.M). Each dot represents an individual measurement value of the NMJ4. The adjusted p-values are indicated on the graph. Two-way ANOVA with Tukey's multiple comparison tests were carried out for the statistical analysis. p-value <0.0001=****, p-value <0.001=***, p-value <0.01=**, p-value <0.05=*. Compared to the wild type, the number of boutons was significantly higher in the null mutant (**A**), the null mutant was enriched for active zones **(B)**, the synaptic area was larger in the null mutant **(C)**, *Top3β*$^{\Delta RGG}$ NMJs displayed the longest branch length **(D)**.

Figure 7:

(a version of Fig. 7 with better resolution and contrast is appended)

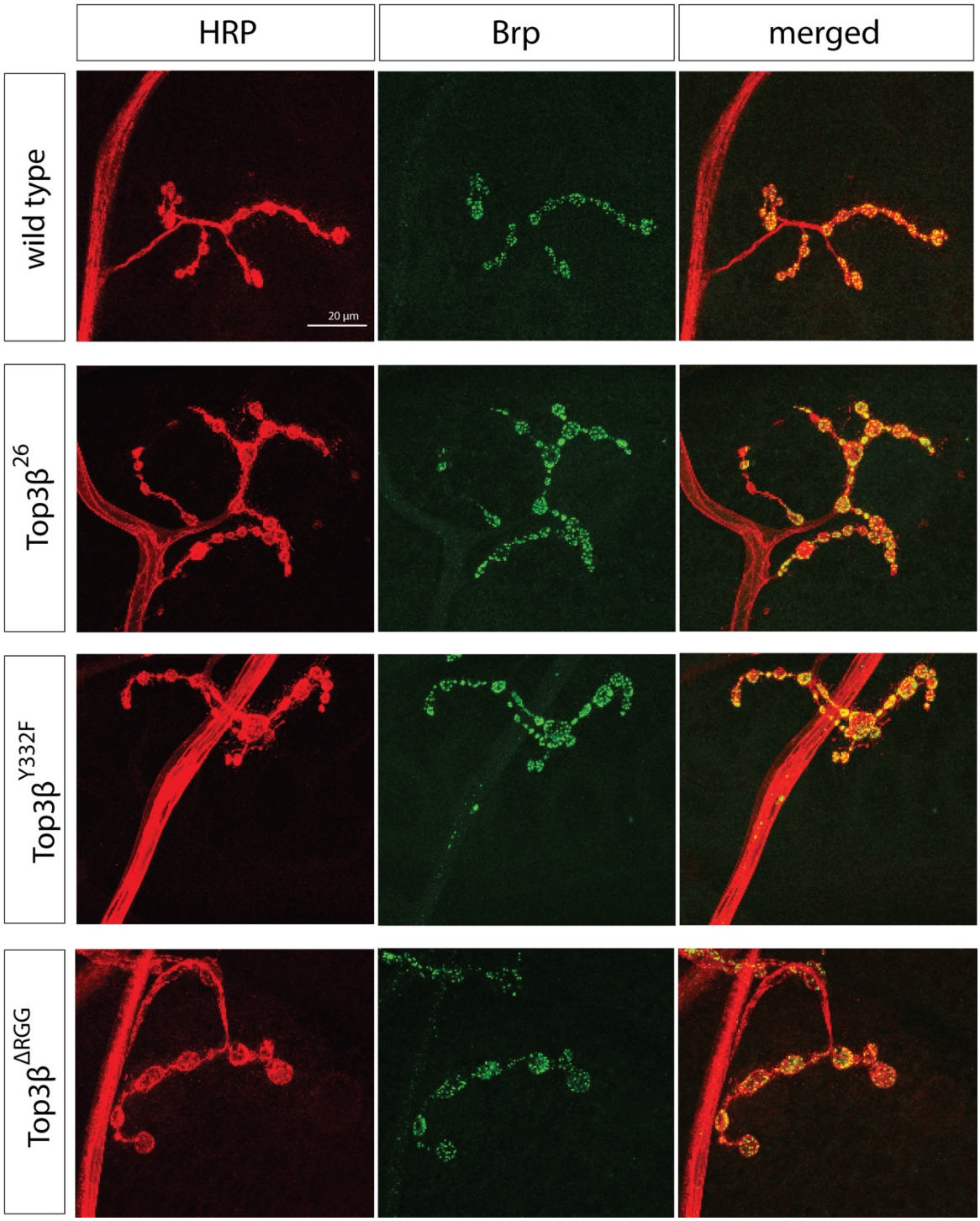

Fig. 7. Morphology of larval NMJs. Representative NMJ 4 synapses (segments A3-A5, both sides) from the wild type and the 3 different *Top3β* mutants double-stained with anti-HRP to visualize the neuronal plasma membrane (red) and anti-Brp (green), which marks active zones. The genotypes are indicated on the left. *Top3β*^{26} is a presumed null mutant. Scale bar is 20µm and magnifications are the same for all panels. All panels show maximum intensity projections with a z-step size of 0.91 µm.

247 the increased elaboration of the NMJs in the null mutant may suggest that a compensatory
248 mechanism exists that attempts to compensate for a less efficient NMJ.

249 The NMJs of the null (*Top3β*^{26}) and the catalytic (*Top3β*^{Y332F}) mutants showed an increased
250 number of satellite boutons **(A in Supplementary Fig. S1)**. Satellite boutons are small boutons
251 that bud from a terminal parent and branching boutons (20). 53% of the *Top3β*^{26} NMJs were
252 found to contain satellite boutons (16 out of 30 images), compared to 27% of *Top3β*^{Y332F} NMJs
253 (8 out of 30 images) and 13% of *Top3β*$^{\Delta RGG}$ NMJs (4 out of 30 images). The wild-type NMJs
254 showed only very few satellite boutons (1 out of 30 NMJ images).

255 The null and the catalytic mutants also displayed filopodial extensions in their NMJs, which
256 mostly stained positive for the active zones in presynaptic neurons using the anti-Bruchpilot
257 (Brp) antibody **(B in Supplementary Fig. S1)**. Filopodial extensions appear as thin, thread-like
258 structures (21). 43% (13 out of 30) of the *Top3β*^{Y332F} mutant NMJs, 30% (9 out of 30) of the
259 *Top3β*^{26} NMJs, and 17% (6 out of 30) of the *Top3β*$^{\Delta RGG}$ NMJs showed such filopodial
260 extensions, while these structures were only seen 3% of the wild-type NMJs (1 out of 30).
261 Such filopodial extensions were either sprouting from the terminal boutons or other more
262 proximal boutons of the axon branches.

263 This NMJ study further showed that among the three mutant alleles, the *Top3β*$^{\Delta RGG}$ mutant
264 displayed a unique feature because it mostly contained by far the longest individual branch
265 **(Figs. 6D)**. This suggests that this mutation hinders the formation of complex branched
266 structures **(Fig. 7)**. Additionally, the terminal boutons in the *Top3β*$^{\Delta RGG}$ mutant were often
267 swollen (**C in Supplementary Fig. 1**; 37% in the Top3β$^{\Delta RGG}$), while they developed normally in
268 the wild-type, *Top3β*^{26}, and *Top3β*^{Y332F} mutants (10% in the wild type, 13% in the *Top3β*^{26}, and
269 10% in the *Top3β*^{Y332F}).

270 ***Deteriorating neuromuscular structure and function in Top3β mutants***

271 The negative geotaxis assay measures the activity of the nervous system and the musculature,
272 and the coordination between them. In this assay, all four genotypes showed similar climbing
273 abilities in young flies **(Fig. 8A).** Neuromuscular conditions sometimes become only apparent
274 at an older age because the young nervous system can compensate for some cellular deficits.
275 But such compensations can take their toll if they stress the cells. We, therefore, tested for
276 premature aging and age-related degeneration of the climbing ability. Indeed, as seen in **Fig.**

Figure 8:

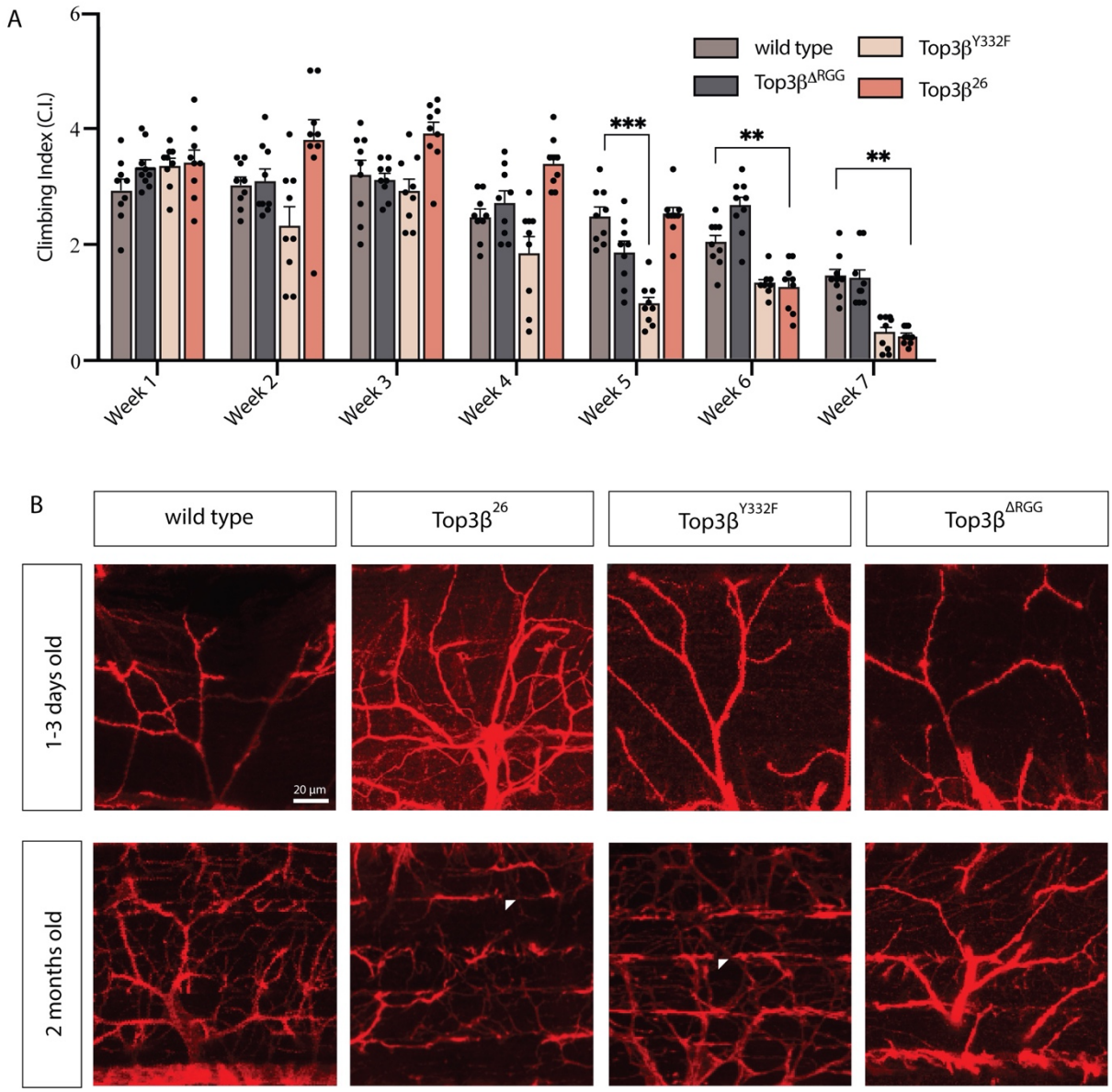

Fig. 8. Aging effects of *Top3β* mutants. A) Climbing assays of wild type, *Top3β*$^{\Delta RGG}$, *Top3β*^{Y332F}, and *Top3β*^{26}. A two-way ANOVA analysis was performed. The graph bars show the mean climbing index (C.I.) for the different genotypes. Error bars represent the standard error of the mean (S.E.M). Each dot represents a calculated individual C.I. The adjusted p-values for each significant difference are indicated on the graph. (p-value <0.0001=****, p-value <0.001=***, p-value <0.01=**, p-value <0.05=*.) B) In adults, null mutant NMJs contain more branches than the wild type, indicative of a compensatory mechanism. Arrowheads point to loss of synaptic integrity of dorsal longitudinal flight muscle (DLM) NMJ synapses visualized by structural staining of motor neurons. The progressive denervation of the DLM is seen particularly in the null and the *Y332F* mutant in the adult thoracic NMJs. Scale bar, 20µm. All panels show maximum intensity projections with a z-step size of 0.7 µm.

277 **8A,** from week 6 on, the *Top3β*^{Y332F} and *Top3β*^{26} flies became slower, and their climbing ability
278 declined more than the wild-type one. The results suggest that Top3β plays a crucial role in
279 aging and combating neurodegeneration in *Drosophila* motor neurons. As the flies age, their
280 motor abilities and neurotransmission decline, and fragmentation of synaptic motor
281 terminals becomes apparent (22).

282 To gain insights into the possible adaptation of the adult neuromuscular system, we also
283 studied the structure of the adult NMJs in the four genotypes during aging **(Fig. 8B)**. The young
284 null mutants (followed by *Top3β*^{Y332F} and *Top3β*$^{\Delta RGG}$) had more branched structures compared
285 to the simpler branch structures in the wild type. As suggested for the larval NMJ, the
286 observed overgrowth might have arisen to compensate for suboptimal synaptic physiology.
287 However, as the flies age, progressive denervation of the DLM (Dorsal Longitudinal Muscles)
288 synapses in the null mutant occurred, leading to a progressive loss of locomotive ability and
289 more rapid aging **(Fig. 8B).** In both the null and *Top3β*^{Y332F}, a loss of synaptic integrity was
290 observed during aging in 1-2 months old flies **(Fig. 8B)**. Because *Top3β*^{26} and *Top3β*^{Y332F} flies
291 live less long than wild-type and *Top3β*$^{\Delta RGG}$ flies **(Supplementary Fig. S2)**, the decline of their
292 NMJ structure and function is most likely even stronger than observed in the living animals.
293 Furthermore, the similarity between the phenotypes of *Top3β*^{26} and the *Top3β*^{Y332F} flies, the
294 effect on longevity and aging seems to be caused primarily due to the loss of the enzymatic
295 activity of Top3β, which leads to loss of synaptic integrity, faster aging, and shortened
296 lifespan.

297

298 **Discussion**

299 ***RNA targets of Top3β***

300 Finding that Top3β interacts with splicing factors **(Figs. 3, 4)** appears to be a significant result
301 because Top3β's RNA targets have a greater number of exons and alternative transcripts
302 **(Figs. 1E, F)**. Exon numbers and intron length also correlate with alternative splicing (AS)
303 (23)(24)(25)(26)(27) and Drosophila Top3β also interacts more frequently with RNAs that
304 contain longer introns **(Fig. 1D)**. Moreover, snoRNAs are also enriched in the Top3β targets
305 and recent studies showed that snoRNAs play an essential role in the regulation of mRNA
306 splicing and editing and they are also involved in stress response and metabolic homeostasis
307 (28), two additional characteristics of Top3β targets.

308 Transcripts from neural genes were also enriched among the Top3β targets. Alternative
309 splicing of precursor mRNA is a crucial step of gene expression that increases transcriptomic
310 and proteomic diversity and must be tightly regulated during neurodevelopment (29). The
311 nervous system exhibits extraordinarily complex and diverse AS patterns in a variety of
312 metazoan organisms (30)(31)(32)(33). Importantly, these diversified AS patterns play
313 essential roles in modulating numerous neuronal states and activities (34)(35). Neurons are
314 susceptible to splicing perturbations with numerous neurological diseases linked to splicing
315 defects.

316 Top3β has been associated with many neurodevelopmental and neurodegenerative diseases,
317 including schizophrenia, autism spectrum disorders, and Fragile X syndrome. A previous study
318 showed that autism risk factor genes are exceptionally long (36). Longer genes tend to have
319 more splice variants (37) and have greater numbers of regulatory elements (38). Longer pre-
320 mRNAs provide more chances for splicing errors (because of the increased difficulty to
321 identify the correct splice sites) but also for entanglement. The latter is also a considerable
322 problem during transport over extended distances, which might even involve mRNA
323 packaging and unpackaging before the mRNAs can be activated for translation at the right
324 place and at the right time. During such transport, long linear molecules, such as mRNAs, are
325 likely to become entangled or suffer other structural problems that might interfere with their
326 transport or translation. The coding sequence (CDS) and untranslated regions (UTRs) of an
327 mRNA molecule are also important for regulating gene expression at the level of splicing, RNA

328 localization, and protein synthesis. UTRs affect not only the translation in neurons but also
329 the localization to the places where these mRNAs will be translated in response to extrinsic
330 stimuli, such as neurotrophins, synaptic activation, and regeneration after injury
331 (39)(8)(40)(41). Consistent with the proposed function of Top3β in rescuing (pre-)mRNAs with
332 the described characteristics, the embryonic targets of Top3β displayed a strong bias for these
333 characteristics (**Figs. 1C-F**).

334 ***Important target genes of Top3β***

335 Lack of the enzymatic activity of Top3β causes the formation of many satellite boutons in the
336 NMJs**.** These tiny boutons represent a developmentally arrested stage of bouton maturation
337 (20), pointing to the importance of the catalytic activity of Top3β for NMJs maturation.
338 Identifying Top3β targets suggested that mRNAs encoding large cytoskeletal and cortical
339 elements (*kst*, *α-spec*, *shot, mgl*), regulators of NMJ growth (*Prosap*), and sufficient functional
340 mitochondria are important to overcome this developmental block. The latter is also
341 interesting because impairment of the mitochondrial one-carbon metabolism has been linked
342 to an increase in the number of satellite boutons (42). An interesting Top3β target is the *shot*
343 mRNA, which encodes a large cytoskeletal linker molecule that participates in axon growth
344 and neuromuscular junction maintenance (43). *shot* promotes the formation of F-actin-rich
345 filopodia at growth cones of *Drosophila* primary neurons (44), and proper F-actin dynamics is
346 essential for axon guidance (45). Impaired *shot* function leads to excessive growth at the larval
347 NMJ (46). *shot* produces 22 transcript isoforms, which is many more than the average of 2
348 isoforms per *Drosophila* gene. *shot* RNA and protein expression in embryos are markedly
349 reduced and less localized in null mutant and *Top3β*^{Y332F} embryos. The enzymatic activity of
350 Top3β is therefore key to the proper expression of *shot* mRNA and protein, pointing to its
351 possible involvement in splicing *shot* pre-mRNAs, resolving RNA entanglements, and
352 translation into the protein.

353 Along with α-Spec, Kst (β_H-Spectrin) crosslinks F-actin and acts as a molecular scaffold (47)
354 when it is recruited to the apical membrane of epithelial cells (48). The mRNAs encoding these
355 two proteins are both targets of Top3β, and we showed that the normal expression levels and
356 localization of the Kst protein in the embryos depend on the enzymatic activity of Top3β,
357 suggesting again that the lack of Top3β reduces the translation of *kst* mRNA at the pre- mRNA

358 or mRNA level. Interestingly, Top3β accumulates also preferentially at the apical cortex of
359 embryos, further suggesting that higher Top3β activity in this location may contribute to the
360 apical translatability of apical transcripts, thereby expressing the encoded protein in this
361 location at higher levels, even if the mRNA is uniformly expressed. It thus appears that
362 subcellular localization of Top3β activity might even serve as a novel tool to target gene
363 expression to specific cellular locations even if its mRNA is expressed uniformly.

364 Finally, we investigated Dhc, the large heavy chain subunit of the cytoplasmic dynein motor
365 complex (40)(41). Being the major retrograde motor in all cells, neuronal cytoplasmic dynein
366 moves cargo from the synapse along the axon and back to the cell body (49). During
367 Drosophila oogenesis, dynein transports mRNAs, proteins, and organelles from the nurse cells
368 into the oocyte, where they are deposited for the young embryo. In the embryo, it then
369 transports them to the apical cortex. We observed reduced protein expression and lack of
370 Dhc concentration at the apical cortex in both the null and *Top3β*^{Y332F} embryos. Again, *Top3β*
371 and its enzymatic activity are needed to allow proper protein expression and the
372 establishment of the polar distribution of Dhc with its apical accumulation.

373 The RGG box of Top3β appeared to be less important for most phenotypes analyzed. An
374 exception was that the deletion of this box caused overgrowth of the longest branch in NMJs
375 and a swollen last bouton phenotype, a phenotype that had been ascribed to defective
376 retrograde microtubule-dependent transport because it was observed in the *p150*^{Glued} CAP-
377 Gly domain mutant where the altered dynactin activity caused the loss of the retrograde
378 transport activity. As a consequence, cell components and proteins accumulated at synaptic
379 termini leading to overgrowth of the NMJs and swollen last boutons (50). Normally, Dhc
380 transports many RNAs and proteins as part of the Dynein/Dynactin (*p150*^{Glued})/BicD transport
381 (DDB) machinery. We found that the RGG deletion also reduced the binding of Top3β to the
382 motor protein Dhc **(Supplementary Table S8)**. If the lack of Top3β or its removal from the
383 terminal bouton by retrograde transport is important to terminate the bouton growth at the
384 right size, we can hypothesize why Dynein/Dynactin transport is needed and why only the
385 RGG mutant and not the *Top3β* null mutant shows the swollen bouton and phenotype. There
386 is good evidence that a physical interaction between Top3β and the dynein motor happens
387 and is important for normal cargo localization. Top3β forms a complex with Tdrd3 and FMR1
388 and the latter was shown to interact with the BicD, the subunit of the DDB transport

389 machinery, and to depend on this interaction to be transported normally along microtubules
390 and to accumulate at the proper levels and locations in the nervous system (1)(51). The
391 Top3β$^{\Delta RGG}$ protein would then be expected to stay longer in the terminal bouton and further
392 facilitate the expression from its target mRNAs of factors that promote branch and bouton
393 growth.

394 There is another phenotype that shows the importance of the RGG box for the localization of
395 Top3β. It is needed for the nuclear localization of a good fraction of Top3β in the blastoderm
396 embryo **(Fig. 5)**, a process that might also involve dynein transport. The failure of the
397 Top3β$^{\Delta RGG}$ mutant protein to localize to the embryonic nuclei additionally suggests that
398 reduced nuclear functions of Top3β$^{\Delta RGG}$ might contribute more to the *Top3β*$^{\Delta RGG}$ mutant
399 phenotype.

400 ***Top3β environment and relevance***

401 Stress granules (SGs) are essential for normal cell functioning when cells are subjected to
402 stress stimuli. SGs can be seen to assemble under different conditions, such as oxidative
403 stress, the presence of translation-blocking drugs, viral infection, and the knockdown of
404 specific translation initiation factors (52). When the cellular stress state is persistent, SGs alter
405 multiple intracellular signaling pathways so that cells can adjust their metabolism and even
406 cellular architecture to survive (53)(54). If the SGs persist for the long term in cells, their
407 susceptibility to aging or aging-related diseases (neurodegenerative disorders) increases (55).
408 Moreover, mRNA accumulation in stress granules correlates with longer coding and UTR
409 regions, and poor translatability (56), further suggesting that longer RNAs are more likely to
410 cause cellular stress. Gene ontology analysis on the stress granule mRNAs showed gene
411 enrichment in ATP binding, transcription factors, RNA splicing, and cell cycle factors (57). The
412 enrichment of SGs in our gene ontology results suggests a role for Top3β in storing or
413 recovering mRNAs during periods of stress, which includes neurodegeneration and aging.

414 The enrichment of RNAs encoding neuronal ribonucleoproteins (RNP) particles, also known
415 as granules, was a common result among our Top3β targets from heads and embryos. These
416 RNP granules concentrate specific sets of mRNAs and regulatory proteins in the same
417 location, promoting their common long-distance transport to axons or dendrites (20)(21).
418 They also have a dual function in regulating the translation of associated mRNAs while

419 preventing the translation of others (58). As a component of neuronal RNPs, Me31B mediates
420 the transport and controls the translation of neuronal RNAs, including the translational
421 repression of synaptic transcripts (26). We found Me31B highly enriched with Top3β and this
422 interaction depended on the RGG box, suggesting that the RGG box links Top3β to the
423 neuronal RNPs.

424 Mitochondrial dysfunction is another factor that can negatively affect neuron development
425 as neurons require a high energy supply and have limited regenerative capabilities. The Krebs
426 or tricarboxylic acid (TCA) cycle is a crucial metabolic pathway that integrates various
427 mitochondrial functions and has been implicated in aging, neurodegeneration, and cancer
428 (23)(59)(60). The high presence of TCA process components and one-carbon metabolism
429 elements associated with Top3β suggest that Top3β may also play a role in aging through the
430 regulation of mitochondrial activity.

431 The malfunctioning of numerous cellular mechanisms can cause neuronal activities to be less
432 efficient and produce cellular stress. Further research needs to test, which of the individual
433 pathways suggested by our work causes a physiological problem in the human conditions
434 mentioned in this discussion. However, serious health issues often arise when several
435 pathways are not functioning properly anymore, making it difficult to pinpoint the primary
436 cause. Our work also revealed that reduced activity of Top3β is likely to affect several of the
437 pathways that rely on Top3β because under limiting amounts of Top3β, elevated stress in one
438 pathway will further reduce limited Top3β, affecting the less sensitive pathways as well. The
439 combination of defects in the different Top3β pathways is, therefore, likely to contribute
440 significantly to the outcome of the various neurodevelopmental and cognitive disorders
441 *Top3β* has been implicated in.

442

443 ## Material and Methods

444 ### Fly stocks and maintenance

445 The *white* (*w)* strain was used as a wild-type control as this was the genetic background of the
446 mutants used in this study. The mutant fly stocks *Top3β*^{Y332F} and *Top3β*$^{\Delta RGG}$ were established
447 as described below. *Top3β*^{26} was from Lee and colleagues (61). The fly stocks were grown and
448 maintained on a regular corn medium (ingredients: corn, yeast powder, sucrose syrup, agar,
449 potassium sodium tartrate tetrahydrate, water, nipagin, and propionic acid) supplied with
450 brewer's yeast for the experiments. All *Drosophila melanogaster* fly stocks were stored at
451 18°C in glass or plastic vials with day/night (12 h/12 h) light cycles. All experiments were
452 performed at 25°C.

453 ### Generation of *Top3β* alleles:

454 Genomic sequences were scanned for suitable sgRNA target sites with the JBrowse from
455 FlyBase and appropriate sgRNA sequences were chosen based on (a) their distance from the
456 tagging site, and (b) the absence of potential off-target sites on the same chromosome as the
457 target site (62). To mutate the endogenous *Top3β*, a sgRNA was designed, which hybridized
458 in the vicinity of the Y332 codon of *Top3β* and induced the Cas9 nuclease to perform a double-
459 strand break. Complementary oligodeoxynucleotides with suitable overhangs
460 (**Supplementary Table S7**) were annealed and cloned into the pCFD5 vector, which is used to
461 express the sgRNA (63). The Cas9 fly stock was obtained from the Bloomington stock center
462 (ref. number: 79004). ssDNA was designed for the mutation changing the Tyr (Y) to a Phe (F)
463 codon and injected into the progeny produced by Cas9- and sgRNA-expressing flies. The
464 single-strand oligodeoxynucleotide with the flanking arms precisely matching the
465 endogenous sequences changes the sequence at the mutation site by serving as a template
466 (**Supplementary Table S7**) for the homologous recombination DNA repair at the double-
467 strand break. The same strategy was used to delete the endogenous RGG region in *Top3β*
468 (ΔRGG) using the appropriate gRNA and ssDNA templates.

469 ### Generation of the *Top3β::eGFP* cDNA clone for GAL4>UAS expression

470 For the *Top3β::eGFP* construct, the *Top3β* cDNA clone LD10035 was amplified. Enhanced GFP
471 (EGFP) was PCR amplified from a plasmid (pEGFP–C3). PCR amplified fragments were run on

472 an agarose gel and purified using the Wizard SV kit (Promega). The sequences were cloned
473 into the pUASz1.0 vector (64) with the *eGFP* ORF at the C-terminal end of the *Top3β* ORF using
474 a ligation kit (NEB). The UASz vector allows one to induce the constructs in any tissue,
475 including the somatic tissue, the germline, and the CNS (64). Plasmids were sequenced to
476 confirm the integrity of the construct and purified with a PureYield kit (Promega) for injection.
477 Transgenic stocks were established with the attP landing platform 86F from the Bloomington
478 stock center (ref. number: 24749).

479 To generate an enzymatically dead enzyme, a Phe codon substituted the codon for the Tyr
480 responsible for crosslinking the enzyme with the nucleic acid in the *UASz-Top3β::eGFP* vector
481 to give rise to *UASz-Top3β*^{Y332F}*::eGFP*. Similarly, to figure out the role of the RGG box, we
482 deleted the gene DNA coding for this box in the *UASz-Top3β::eGFP* vector, giving rise to *UASz-*
483 *Top3β*$^{\Delta RGG}$*::eGFP*. At the site of the desired mutation, oligonucleotide primers with the
484 desired mutation were used to amplify the mutant double-stranded DNA plasmid
485 (**Supplementary Table S7)**. A protocol based on two different PCR amplifications was used for
486 this. First, two elongation reactions were carried out, with one of the two primers each. In
487 the second reaction, the two initial elongation reactions were mixed and an additional PCR
488 reaction was carried out. The wild-type and mutant eGFP fusion constructs were transformed
489 into *Drosophila* using the attP-86F landing platform. mat-tub-Gal4 (ref. number: 7062) was
490 used to drive the expression in the older female germline and Gal4-BG380 (ref. number:
491 24749) to drive expression in the CNS. UASz-eGFP transgenic flies, obtained from the
492 Bloomington stock center, were used as negative controls.

493 **Sample preparation for mass spectrometry**

494 Drosophila Top3β was purified using Top3β tagged with eGFP. The eGFP tag combined with a
495 mouse anti-eGFP antibody has proven to work extremely well for protein-IPs (65). Protein G
496 magnetic beads were washed 3x with PBS and incubated for 2 hours with an anti-GFP
497 antibody. After this, they were washed 3x with 1 ml 1x PBS and one more time with 1 ml
498 homogenization buffer (25 mM Hepes PH 7.4; 150 mM NaCl; 0.5 mM EDTA PH 8.0, 1 mM DTT,
499 protease inhibitors). To prepare the extracts, 1 ml homogenization buffer was added to 1 gr
500 of the samples (dechorionated embryos 0-2 hours or adult heads 1-5 days old) in the glass
501 homogenizer. The samples were homogenized and transferred into the tube. Homogenized
502 samples were centrifuged at 16,000 g (RCF), 4°C for 40 min. The interphase was transferred

503 into a fresh Eppendorf tube, centrifuged again at 16,000 g, 4°C for 40 min, and transferred
504 into a fresh tube. Beads were then incubated with the extracts for 6 hours at 4°C on a wheel.
505 Extracts were then removed from the beads. The beads were washed once with 1 ml
506 homogenization buffer and then several times with wash buffer (25 mM Hepes PH 7.4; 150
507 mM NaCl; 0.5 mM EDTA PH 8.0; 1 mM DTT; protease inhibitors). The wash buffer was
508 removed, and the beads were sent for mass spectrometry.

509 **Mass spectrometry**

510 Mass spectrometry analysis was done by the Proteomics and Mass Spectrometry Core Facility,
511 University of Bern, and the data are available in **Supplementary Table S5, S6**. Proteins in the
512 affinity pull-down were re-suspended in 8M Urea / 50 mM Tris-HCl pH8, reduced for 30 min
513 at 37°C with 0.1M DTT / 100 mM Tris-HCl pH8, alkylated for 30 min at 37°C in the dark with
514 IAA 0.5M / 100 mM Tris-HCl pH8, dilute with 4 volumes of 20 mM Tris-HCl pH8 / 2 mM CaCl2
515 before overnight digestion at room temperature with 100 ng sequencing grade trypsin
516 (Promega). Samples were centrifuged, and a magnet holder trapped the magnetic beads to
517 extract the peptides in the supernatant. The digests were analyzed by liquid chromatography
518 (LC)-MS/MS (PROXEON coupled to a QExactive mass spectrometer, ThermoFisher Scientific)
519 with three injections of 5 µl digests. Peptides were trapped on a µPrecolumn C18 PepMap100
520 (5 µm, 100 Å, 300 µm×5 mm, ThermoFisher Scientific, Reinach, Switzerland) and separated
521 by backflush on a C18 column (5 µm, 100 Å, 75 µm×15 cm, C18) by applying a 60 min gradient
522 of 5% acetonitrile to 40% in water, 0.1% formic acid, at a flow rate of 350 ml/min. The Full
523 Scan method was set with a resolution at 70,000 with automatic gain control (AGC) target of
524 1E06 and a maximum ion injection time of 50 ms. The data-dependent method for precursor
525 ion fragmentation was applied with the following settings: resolution 17,500, AGC of 1E05,
526 maximum ion time of 110 milliseconds, mass window 2 m/z, collision energy 27, underfill ratio
527 1%, charge exclusion of unassigned and 1+ ions, and peptide match preferred, respectively.

528 The data were then processed with the software MaxQuant (66) version 1.6.14.0 against the
529 UniProtKB(67) Drosophila 7228 database (release 2021_02) containing canonical and isoform
530 entries, to which common contaminants were added. The following parameters were set:
531 digestion by strict trypsin (maximum three missed cleavages), first search peptide tolerance
532 of 15 ppm, MS/MS match tolerance of 20 ppm, PSM and protein FDR set to 0.01 and a
533 minimum of 2 peptides requested per group. Carbamidomethylation on cysteine was selected

534 as a fixed modification; the following variable modifications were allowed: methionine
535 oxidation, deamidation of asparagines and glutamines, and protein N-terminal acetylation; a
536 maximum of 3 modifications per peptide was allowed. Match between runs was turned on
537 (match time windows 0.7 min) but only allowed within replicates of the same kind.

538 Peptides were normalized by variance stabilization (68), imputed and combined to form Top3
539 (69) intensities, and considered alongside MaxQuant's Label-Free Quantification (LFQ) values.
540 Missing peptides, respectively LFQ intensities, were imputed by drawing values from a
541 Gaussian distribution of width 0.3 centered at the sample distribution mean minus 2.5x the
542 sample standard deviation, provided there were at most 1 non zero value in the group;
543 otherwise, the Maximum Likelihood Estimation (70) was used. Differential expression was
544 performed by applying the empirical Bayes test (71) between groups; significance testing was
545 performed as described (72).

546 **RNA immunoprecipitation**

547 Protein G magnetic beads were washed 2-3x with 1ml blocking buffer (20 mM Hepes, 150
548 mM KCl, 20% Glycerol, 0.5 % Tween, BSA (Biolabs), Heparin 0.2 mg/ml, SDS 0.1%, 1/2 pill EDTA
549 free protease inhibitors). Beads were blocked with a blocking buffer for 2-3 hours at room
550 temperature. An anti-GFP antibody was added to the beads and rotated for 1-2 hours. Beads
551 were washed 3x with non-hypotonic lysis buffer (20 mM Hepes, 1 mM EDTA, 150 mM KCL, 1
552 mM DTT, 0.5% Tween, 20% glycerol, SDS 0.1%, 1/2 pill EDTA free protease inhibitors). Anti-
553 GFP antibody was added to the beads and rotated for 1-2 hours at room temperature. Beads
554 were washed 3x with non-hypotonic lysis buffer.

555 Fly heads were collected from 1-5 days old adults. Dechorionated embryos were 0-2 hours
556 old. 1g of the extracts homogenized in 2 ml hypotonic lysis buffer (20 mM Hepes, 10 mM KCL,
557 1 mM EDTA, 1 mM DTT, 0.5% Tween, SDS 0.1%, 1/2 pill EDTA free protease inhibitors, and
558 RNase inhibitor (Biolabs, 40,000U/ml)). 600 μl of extract, 323 μl of Adjusting buffer (57%
559 Glycerol 100%, 0.4M KCl, 1 mM EDTA, 1 mM DTT, 20 mM Hepes, SDS 0.1%), and 2 μl of RNase-
560 free DNase I (20 μ/ml, Roche) were added to the washed antibody beads and were
561 precipitated ON rotating at 4°C. Samples were washed 8x with 1 ml high salt wash buffer (20
562 mM Hepes, 1 mM EDTA, 200 mM KCl, 1 mM DTT, 0.5% Tween, 20% Glycerol, SDS 0.1%, 1/2
563 pill EDTA free protease inhibitors, and RNase inhibitor (Biolabs, 40,000U/ml)). On the last

564 wash, 100 μl of the samples were taken before centrifugation. 100 μl of proteinase K buffer,
565 1.5 μl proteinase K (20 mg/ml Roche), and μl RNase inhibitor was added to each tube and
566 were incubated for 30min at 55°C. 1 ml Trizol reagent was added to each tube, and RNA was
567 extracted according to the Trizol protocol (TRIzol™ Reagent, Invitrogen™, Catalog number:
568 15596026).

569 The Next Generation Sequencing Platform, University of Bern, conducted quality control
570 assessments, library generation, sequencing runs, and sequencing quality control steps. The
571 quantity and quality of the purified total RNA were assessed using a Thermo Fisher Scientific
572 Qubit 4.0 fluorometer with the Qubit RNA BR or HS Assay Kit (Thermo Fisher Scientific,
573 Q10211 or Q32855, respectively) and an Advanced Analytical Fragment Analyzer System using
574 a Fragment Analyzer RNA Kit (Agilent, DNF-471), respectively. Sequencing libraries were made
575 using a CORALL Total RNA-Seq Library Prep Kit, Version 1 with UDI 12nt Set A1 (Lexogen,
576 117.96) according to Lexogen's guidelines for this kit. Pooled cDNA libraries were paired-end
577 sequenced using either shared Illumina NovaSeq 6000 SP, S1, or S2 Reagent Kits (200 cycles;
578 Illumina, 200240719, 2002831, or 20028315) on an Illumina NovaSeq 6000 instrument. The
579 quality of the sequencing run was assessed using Illumina Sequencing Analysis Viewer
580 (Illumina version 2.4.7) and all base call files were demultiplexed and converted into FASTQ
581 files using Illumina bcl2fastq conversion software v2.20.

582 The quality of the RNA-seq reads was assessed using fastqc v0.11.9 (73) and RSeQC v4.0.0
583 (74). Unique molecular identifiers (UMI) were extracted with umi-tools v1.1.2 (75), and
584 adapters were trimmed with cutadapt v3.4.1 (76) according to manufacturer instructions. The
585 reads were aligned to the Drosophila reference genome (BDGP6.32) using hisat2 v2.2.1 (77).
586 FeatureCounts v2.0.1 (78) was used to count the number of reads overlapping with each gene
587 as specified in release 103 of the Ensembl genome annotation. The Bioconductor package
588 DESeq2 v1.36.0 (79) was used to test for differential gene expression between the
589 experimental groups. To generate the log2 fold change versus transcript length plots, the
590 estimated log2 fold change per gene was plotted against the most extended transcript length
591 per gene with R v4.2.1 (80). We used the log2 fold change>=1 and the adjusted p-value (adjp-
592 value) <0.05 of enrichment over control for further analysis.

593

594 **Dissection and immunostaining of third-instar larvae**

595 Male and female wild-type, *Top3β*^{Y332F}, *Top3β*$^{\Delta RGG}$, and *Top3β*^{26} third instar wandering larvae
596 (approximately 94 hours old) were dissected in 1x PBS (Phosphate Buffer Saline). After
597 removing the internal organs, the fillets were washed 3x with PBS to remove all residual tissue
598 parts. The fillets were then fixed in 4% paraformaldehyde (PFA) for 15 min, rinsed in PTX (PBS
599 + 0.1% Triton X- 100), and blocked in PTX + 5% NGS (normal goat serum) to block unspecific
600 binding sites. After blocking for 1 hour, the fillets were stained with the primary antibodies
601 rabbit anti-HRP (1:750 dilution) from Jackson Immuno Research and mouse anti-Brp (nc82;
602 1:125 dilution) from Developmental Studies Hybridoma Bank. The fillets were then incubated
603 overnight at 4°C on a Nutator. The next day, the unbound antibodies were washed off with
604 500 µl of PTX (4x) for one hour. The secondary antibodies, goat anti-rabbit A488 (1mg/ml;
605 diluted 1:200; LubioScience GmbH) and goat anti-mouse A647 (1.5 mg/ml; diluted 1:200;
606 Jackson ImmunoResearch Laboratories Inc.) were added to the fillets and incubated for one
607 hour at room temperature on a Nutator, followed by washing 4x with PTX. The fillets were
608 then incubated with Rhodamine-phalloidin (1 unit/ml; Invitrogen) in 1x PBS for 15 minutes to
609 stain the larval muscles' F-actin. The fillets were then rinsed, washed with 1x PBS, and placed
610 into 70% glycerol (in 1x PBS) in Eppendorf tubes. These were wrapped with foil paper and
611 kept at 4°C until they settled down at the bottom of the tubes, Then, they were mounted on
612 slides. Focusing on abdominal segments A3-A5, we produced a collection of a total of 120
613 NMJ images to analyze synaptic morphology. These were quantified using the macro
614 *'Drosophila_NMJ_morphometrics'*c (19).

615 **Image acquisition**

616 The NMJ terminals of muscle 4 of the abdominal hemisegments 3, 4, and 5 on the left and
617 right sides were imaged using a Leica SP8 confocal microscope. 2-channel image stacks of the
618 NMJ terminals were acquired using a 63x objective and a z-step size of 0.91 µm. The acquired
619 images were exported as individual .tiff files.

620 **A Fiji macro for multiparametric larval NMJ analysis**

621 The macro *'Drosophila_NMJ_morphometrics'* runs on Fiji and quantitatively assesses nine
622 morphometric characteristics of many glutamatergic NMJs based on high-content confocal
623 microscopy images. The macro accurately assessed the following eight characteristics: NMJ

624 area, perimeter, total length, longest branch length, number of islands, number of branches
625 and branching points, and number of active zones. This made them suitable for high-
626 throughput analyses of synapse morphology. The macro gave an inaccurate count of the
627 number of boutons, so the boutons were counted manually. The images were run on the
628 algorithm and were processed to a result picture in which the delineation of the automatically
629 recognized NMJ features was presented. The macro "Drosophila NMJ Morphometrics" was
630 downloaded (https://doi.org/10.6084/m9.figshare.2077399.v121). This macro is compatible
631 with Fiji (ImageJ) version 1.49k. All images were analyzed with this algorithm and the results
632 were visualized in GraphPad Prism 8.

633 **Dissection and immunostaining of adult Dorsal Longitudinal Muscles (DLMs)**

634 Thoraces of 0-3 days old and 2 months old adult wild-type, *Top3β*^{Y332F}, *Top3β*$^{\Delta RGG}$, and *Top3β*^{26}
635 flies were separated from the rest of the body in 1x PBS. The thoraces were fixed in PFA (32%
636 formaldehyde diluted to 4% with 1x PBS) for 30 min at room temperature and then washed
637 3x with PBS. All 1x PBS from tubes was removed using a Pasteur pipette. The tubes were
638 submerged into a liquid nitrogen flask for 10 s using cryogenic tweezers. Then, 300 µL of ice-
639 cold 1x PBS was added to the samples. The thoraxes were cut into two hemithoraces and
640 transferred into 1x PBS (22) and blocked in 1x PBS with 0.1% normal goat serum and 0.2%
641 Triton X-100 at pH 7.4 for at least one h at 4°C. Mouse anti-Brp (nc82; 1:125 dilution) from
642 Developmental Studies Hybridoma Bank and Phalloidin-647 at a dilution of 1:1,000 in blocking
643 buffer were used to stain motor neurons and muscle tissues, respectively. Primary antibodies
644 were removed on the following day and the tissue was washed four times with PBST for 5 min
645 each on a rotator. For the secondary antibody staining, goat anti-mouse A647 (1.5 mg/ml,
646 diluted 1:200 dilution; Jackson ImmunoResearch Laboratories Inc.) was added to the samples,
647 which were then kept at room temperature for 2 hours in a dark box on the rotator. After the
648 2 h incubation, the secondary stain was washed out 4 times for 5 min with PBST. Then, the
649 samples were mounted on a slide (22).

650 **Negative geotaxis (climbing) assays**

651 Wild-type flies and the three *Top3β* mutant strains were reared on fresh food and allowed to
652 hatch at 25° C. For each genotype, all 0-3 days old adult male flies were collected. Ten young
653 adult male flies, each, were anesthetized and placed in 4 separate graduated glass cylinders

654 with a flat bottom. After 1 hour of recovery from CO_2 exposure, flies were gently tapped 4x
655 to the bottom of the cylinder to startle them repeatedly with constant force to displace the
656 flies to the bottom surface. The flies were then allowed to climb the wall until they reached
657 the top of the column. The climbing procedure was video recorded using an iPhone 11 Pro.
658 These assays were repeated every week over 7 weeks on the same weekday. Three fly
659 batches, each, provided the material for the triplicates which were performed within 5min
660 intervals. After the three trials, each batch of 10 flies was transferred into glass vials and kept
661 at 25° C. Before the experiment, every single batch was inspected to ensure that all 40 flies
662 could be video tracked when they started to climb after the tapping. To calculate each
663 climbing index (CI), flies that remained at the bottom were counted as in zone 0. The formula
664 used to calculate the CI is CI = (0 x n0 + 1 x n1 + 2 x n2 + 3 x n3 + 4 x n4 + 5 x n5) / nTotal,
665 where nTotal is the total number of flies and nx is the number of flies that reached zone x.

666 **Statistics**

667 All statistical analyses were performed using GraphPad Prism 8. The means, standard errors,
668 and p-values for the hatching rate experiments were obtained by one-way ANOVA with
669 Tukey's multiple comparison test. For the multi-parametric quantification of NMJ morphology
670 and the negative geotaxis assays, the means, standard error of the means, and p-values were
671 obtained by two-way ANOVA with Tukey's multiple comparison test.

672

673 **References**

674 1. Xu D, Shen W, Guo R, Xue Y, Peng W, Sima J, et al. Top3β is an RNA topoisomerase
675 that works with fragile X syndrome protein to promote synapse formation. Nat
676 Neurosci. 2013;16(9):1238.

677 2. Ahmad M, Shen W, Li W, Xue Y, Zou S, Xu D, et al. Topoisomerase 3β is the major
678 topoisomerase for mRNAs and linked to neurodevelopment and mental dysfunction.
679 Nucleic Acids Res. 2017;45(5):2704–13.

680 3. Kaufman CS, Genovese A, Butler MG. Deletion of TOP3B is associated with cognitive
681 impairment and facial dysmorphism. Cytogenet Genome Res. 2016;150(2):106–11.

682 4. Dekker NH, Rybenkov V V, Duguet M, Crisona NJ, Cozzarelli NR, Bensimon D, et al.
683 The mechanism of type IA topoisomerases. Proc Natl Acad Sci. 2002;99(19):12126–
684 31.

685 5. Baker NM, Rajan R, Mondragón A. Structural studies of type I topoisomerases.
686 Nucleic Acids Res. 2009;37(3):693–701.

687 6. Pommier Y, Sun Y, Shar-yin NH, Nitiss JL. Roles of eukaryotic topoisomerases in
688 transcription, replication and genomic stability. Nat Rev Mol cell Biol.
689 2016;17(11):703.

690 7. Nostramo R, Xing S, Zhang B, Herman PK. Insights into the role of P-bodies and stress
691 granules in protein quality control. Genetics. 2019;213(1):251–65.

692 8. Siaw GE-L, Liu I-F, Lin P-Y, Been MD, Hsieh T. DNA and RNA topoisomerase activities
693 of Top3β are promoted by mediator protein Tudor domain-containing protein 3. Proc
694 Natl Acad Sci. 2016;113(38):E5544–51.

695 9. Nakamura A, Amikura R, Hanyu K, Kobayashi S. Me31B silences translation of oocyte-
696 localizing RNAs through the formation of cytoplasmic RNP complex during Drosophila
697 oogenesis. Development. 2001;128(17):3233–3242

698 10. Wilhelm JE, Buszczak M, Sayles S. Efficient protein trafficking requires trailer hitch, a
699 component of a ribonucleoprotein complex localized to the ER in Drosophila. Dev
700 Cell. 2005;9(5):675–85.

701 11. Barbee SA, Estes PS, Cziko A-M, Hillebrand J, Luedeman RA, Coller JM, et al. Staufen-
702 and FMRP-containing neuronal RNPs are structurally and functionally related to
703 somatic P bodies. Neuron. 2006;52(6):997–1009.

704 12. Liu J, Carmell MA, Rivas F V, Marsden CG, Thomson JM, Song J-J, et al. Argonaute2 is
705 the catalytic engine of mammalian RNAi. Science (80-). 2004;305(5689):1437–41.

706 13. Wang M, Ly M, Lugowski A, Laver JD, Lipshitz HD, Smibert CA, et al. ME31B globally
707 represses maternal mRNAs by two distinct mechanisms during the Drosophila
708 maternal-to-zygotic transition. Elife. 2017;6:e27891.

709 14. Lee J, Yoo E, Lee H, Park K, Hur J-H, Lim C. LSM12 and ME31B/DDX6 define distinct

710 modes of posttranscriptional regulation by ATAXIN-2 protein complex in Drosophila
711 circadian pacemaker neurons. Mol Cell. 2017;66(1):129–40.

712 15. Hillebrand J, Barbee SA, Ramaswami M. P-body components, microRNA regulation,
713 and synaptic plasticity. Scientific World Journal. 2007;7:178–90.

714 16. Ruscica V, Bawankar P, Peter D, Helms S, Igreja C, Izaurralde E. Direct role for the
715 Drosophila GIGYF protein in 4EHP-mediated mRNA repression. Nucleic Acids Res.
716 2019;47(13):7035–48.

717 17. Lee S, Kolodziej PA. Short Stop provides an essential link between F-actin and
718 microtubules during axon extension. Development. 2002;129(5):1195–1204.

719 18. Liu Z, Steward R, Luo L. Drosophila Lis1 is required for neuroblast proliferation,
720 dendritic elaboration and axonal transport. Nat Cell Biol. 2000;2(11):776–83.

721 19. Castells-Nobau A, Nijhof B, Eidhof I, Wolf L, Scheffer-de Gooyert JM, Monedero I, et
722 al. Two algorithms for high-throughput and multi-parametric quantification of
723 Drosophila neuromuscular junction morphology. J Vis Exp Jove. 2017;(123):55395.

724 20. Gatto CL, Broadie K. Temporal requirements of the fragile X mental retardation
725 protein in the regulation of synaptic structure. Development. 2008;135(15):2637–
726 2648.

727 21. Svitkina TM, Bulanova EA, Chaga OY, Vignjevic DM, Kojima S, Vasiliev JM, et al.
728 Mechanism of filopodia initiation by reorganization of a dendritic network. J Cell Biol.
729 2003;160(3):409–21.

730 22. Sidisky JM, Babcock DT. Visualizing synaptic degeneration in adult Drosophila in
731 association with neurodegeneration. JoVE (Journal Vis Exp. 2020;(159):e61363.

732 23. Ast G. How did alternative splicing evolve? Nat Rev Genet. 2004;5(10):773–82.

733 24. Black DL. Protein diversity from alternative splicing: a challenge for bioinformatics
734 and post-genome biology. Cell. 2000;103(3):367–70.

735 25. Budagyan B, Loraine A. Gene length and alternative transcription in fruit fly. In:
736 Proceedings 2004 IEEE Computational Systems Bioinformatics Conference, 2004 CSB
737 2004. IEEE; 2004. p. 515–6.

738 26. McGuire AM, Pearson MD, Neafsey DE, Galagan JE. Cross-kingdom patterns of
739 alternative splicing and splice recognition. Genome Biol. 2008;9(3):1–19.

740 27. Fox-Walsh KL, Dou Y, Lam BJ, Hung S, Baldi PF, Hertel KJ. The architecture of pre-
741 mRNAs affects mechanisms of splice-site pairing. Proc Natl Acad Sci.
742 2005;102(45):16176–81.

743 28. Liang J, Wen J, Huang Z, Chen X, Zhang B, Chu L. Small nucleolar RNAs: insight into
744 their function in cancer. Front Oncol. 2019;9:587.

745 29. Su C-H, Tarn W-Y. Alternative splicing in neurogenesis and brain development. Front
746 Mol Biosci. 2018;5:12.

747 30. Liu G, Beggs H, Jürgensen C, Park H-T, Tang H, Gorski J, et al. Netrin requires focal
748 adhesion kinase and Src family kinases for axon outgrowth and attraction. Nat
749 Neurosci. 2004;7(11):1222–32.

750 31. Wang ET, Sandberg R, Luo S, Khrebtukova I, Zhang L, Mayr C, et al. Alternative
751 isoform regulation in human tissue transcriptomes. Nature. 2008;456(7221):470–6.

752 32. Irimia M, Weatheritt RJ, Ellis JD, Parikshak NN, Gonatopoulos-Pournatzis T, Babor M,
753 et al. A highly conserved program of neuronal microexons is misregulated in autistic
754 brains. Cell. 2014;159(7):1511–23.

755 33. Li YI, Sanchez-Pulido L, Haerty W, Ponting CP. RBFOX and PTBP1 proteins regulate the
756 alternative splicing of micro-exons in human brain transcripts. Genome Res.
757 2015;25(1):1–13.

758 34. Vuong CK, Black DL, Zheng S. The neurogenetics of alternative splicing. Nat Rev
759 Neurosci. 2016;17(5):265–81.

760 35. Norris AD, Calarco JA. Emerging roles of alternative pre-mRNA splicing regulation in
761 neuronal development and function. Front Neurosci. 2012;6:122.

762 36. King IF, Yandava CN, Mabb AM, Hsiao JS, Huang H-S, Pearson BL, et al.
763 Topoisomerases facilitate transcription of long genes linked to autism. Nature.
764 2013;501(7465):58–62.

765 37. Grishkevich V, Yanai I. Gene length and expression level shape genomic novelties.
766 Genome Res. 2014;24(9):1497–503.

767 38. Sugino K, Clark E, Schulmann A, Shima Y, Wang L, Hunt DL, et al. Mapping the
768 transcriptional diversity of genetically and anatomically defined cell populations in
769 the mouse brain. Elife. 2019;8:e38619.

770 39. Han K, Gennarino VA, Lee Y, Pang K, Hashimoto-Torii K, Choufani S, et al. Human-
771 specific regulation of MeCP2 levels in fetal brains by microRNA miR-483-5p. Genes
772 Dev. 2013;27(5):485–90.

773 40. Tushev G, Glock C, Heumüller M, Biever A, Jovanovic M, Schuman EM. Alternative 3'
774 UTRs modify the localization, regulatory potential, stability, and plasticity of mRNAs in
775 neuronal compartments. Neuron. 2018;98(3):495–511.

776 41. Glock C, Biever A, Tushev G, Nassim-Assir B, Kao A, Bartnik I, et al. The translatome of
777 neuronal cell bodies, dendrites, and axons. Proc Natl Acad Sci. 2021;118(43).

778 42. García-Cazorla À, Verdura E, Juliá-Palacios N, Anderson EN, Goicoechea L, Planas-
779 Serra L, et al. Impairment of the mitochondrial one-carbon metabolism enzyme
780 SHMT2 causes a novel brain and heart developmental syndrome. Acta Neuropathol.
781 2020;140(6):971–5.

782 43. Dewey EB, Parra AS, Johnston CA. Loss of the spectraplakin gene Short stop induces a
783 DNA damage response in Drosophila epithelia. Sci Rep. 2020;10(1):1–13.

784 44. Sanchez-Soriano N, Travis M, Dajas-Bailador F, Gonçalves-Pimentel C, Whitmarsh AJ,

785 Prokop A. Mouse ACF7 and drosophila short stop modulate filopodia formation and
786 microtubule organisation during neuronal growth. J Cell Sci. 2009;122(14):2534–42.

787 45. Prokop A, Beaven R, Qu Y, Sánchez-Soriano N. Using fly genetics to dissect the
788 cytoskeletal machinery of neurons during axonal growth and maintenance. J Cell Sci.
789 2013;126(11):2331–41.

790 46. Valakh V, Walker LJ, Skeath JB, DiAntonio A. Loss of the spectraplakin short stop
791 activates the DLK injury response pathway in Drosophila. J Neurosci.
792 2013;33(45):17863–73.

793 47. Bennett V, Baines AJ. Spectrin and ankyrin-based pathways: metazoan inventions for
794 integrating cells into tissues. Physiol Rev. 2001;81(3):1353–92.

795 48. Thomas GH, Williams JA. Dynamic rearrangement of the spectrin membrane skeleton
796 during the generation of epithelial polarity in Drosophila. J Cell Sci.
797 1999;112(17):2843–52.

798 49. Banks GT, Fisher E. Cytoplasmic dynein could be key to understanding
799 neurodegeneration. Genome Biol. 2008;9(3):1–4.

800 50. Lloyd TE, Machamer J, O'Hara K, Kim JH, Collins SE, Wong MY, et al. The p150Glued
801 CAP-Gly domain regulates initiation of retrograde transport at synaptic termini.
802 Neuron. 2012;74(2):344–60.

803 51. Bianco A, Dienstbier M, Salter HK, Gatto G, Bullock SL. Bicaudal-D regulates fragile X
804 mental retardation protein levels, motility, and function during neuronal
805 morphogenesis. Curr Biol. 2010;20(16):1487–92.

806 52. Vanderweyde T, Youmans K, Liu-Yesucevitz L, Wolozin B. Role of stress granules and
807 RNA-binding proteins in neurodegeneration: a mini-review. Gerontology.
808 2013;59(6):524–33.

809 53. Chinta SJ, Lieu CA, DeMaria M, Laberge R, Campisi J, Andersen JK. Environmental
810 stress, ageing and glial cell senescence: a novel mechanistic link to Parkinson's
811 disease? J Intern Med. 2013;273(5):429–36.

812 54. Reinhardt HC, Schumacher B. The p53 network: cellular and systemic DNA damage
813 responses in aging and cancer. Trends Genet. 2012;28(3):128–36.

814 55. Poljšak B, Milisav I. Clinical implications of cellular stress responses. Bosn J basic Med
815 Sci. 2012;12(2):122.

816 56. Khong A, Matheny T, Jain S, Mitchell SF, Wheeler JR, Parker R. The stress granule
817 transcriptome reveals principles of mRNA accumulation in stress granules. Mol Cell.
818 2017;68(4):808–20.

819 57. van Leeuwen W, VanInsberghe M, Battich N, Salmén F, van Oudenaarden A, Rabouille
820 C. Identification of the stress granule transcriptome via RNA-editing in single cells and
821 in vivo. Cell reports methods. 2022;2(6):100235.

822 58. Formicola N, Vijayakumar J, Besse F. Neuronal ribonucleoprotein granules: Dynamic

823 sensors of localized signals. Traffic. 2019;20(9):639–49.

824 59. Briere J-J, Favier J, Gimenez-Roqueplo A-P, Rustin P. Tricarboxylic acid cycle
825 dysfunction as a cause of human diseases and tumor formation. Am J Physiol Physiol.
826 2006;291(6):C1114–20.

827 60. Mishur RJ, Khan M, Munkácsy E, Sharma L, Bokov A, Beam H, et al. Mitochondrial
828 metabolites extend lifespan. Aging Cell. 2016;15(2):336–48.

829 61. Lee SK, Xue Y, Shen W, Zhang Y, Joo Y, Ahmad M, et al. Topoisomerase 3β interacts
830 with RNAi machinery to promote heterochromatin formation and transcriptional
831 silencing in Drosophila. Nat Commun. 2018;9(1):4946.

832 62. Gratz SJ, Rubinstein CD, Harrison MM, Wildonger J, O'Connor-Giles KM. CRISPR-Cas9
833 genome editing in Drosophila. Curr Protoc Mol Biol. 2015;111(1):31–2.

834 63. Port F, Bullock SL. Augmenting CRISPR applications in Drosophila with tRNA-flanked
835 sgRNAs. Nat Methods. 2016;13(10):852–4.

836 64. DeLuca SZ, Spradling AC. Efficient expression of genes in the Drosophila germline
837 using a UAS promoter free of interference by Hsp70 piRNAs. Genetics.
838 2018;209(2):381–7.

839 65. Vazquez-Pianzola P, Adam J, Haldemann D, Hain D, Urlaub H, Suter B. Clathrin heavy
840 chain plays multiple roles in polarizing the Drosophila oocyte downstream of Bic-D.
841 Development. 2014;141(9):1915–26.

842 66. Cox J, Mann M. MaxQuant enables high peptide identification rates, individualized
843 ppb-range mass accuracies and proteome-wide protein quantification. Nat
844 Biotechnol. 2008;26(12):1367–72.

845 67. Consortium U. UniProt: a worldwide hub of protein knowledge. Nucleic Acids Res.
846 2019;47(D1):D506–15.

847 68. Huber W, Von Heydebreck A, Sültmann H, Poustka A, Vingron M. Variance
848 stabilization applied to microarray data calibration and to the quantification of
849 differential expression. Bioinformatics. 2002;18(suppl_1):S96–104.

850 69. Silva JC, Gorenstein M V, Li GZ, Vissers JP. C; Geromanos, SJ Absolute quantification of
851 proteins by LCMSE: A virtue of parallel MS acquisition. Mol Cell Proteomics.
852 2006;5:144–56.

853 70. Silver JD, Ritchie ME, Smyth GK. Microarray background correction: maximum
854 likelihood estimation for the normal–exponential convolution. Biostatistics.
855 2009;10(2):352–63.

856 71. Kammers K, Cole RN, Tiengwe C, Ruczinski I. Detecting significant changes in protein
857 abundance. EuPA open proteomics. 2015;7:11–9.

858 72. Uldry A-C, Maciel-Dominguez A, Jornod M, Buchs N, Braga-Lagache S, Brodard J, et al.
859 Effect of Sample Transportation on the Proteome of Human Circulating Blood
860 Extracellular Vesicles. Int J Mol Sci. 2022;23(9):4515.

861 73. Andrews S. FastQC: a quality control tool for high throughput sequence data.
862 Babraham Bioinformatics, Babraham Institute, Cambridge, United Kingdom; 2010.

863 74. Wang L, Wang S, Li W. RSeQC: quality control of RNA-seq experiments.
864 Bioinformatics. 2012;28(16):2184–5.

865 75. Smith T, Heger A, Sudbery I. UMI-tools: modeling sequencing errors in Unique
866 Molecular Identifiers to improve quantification accuracy. Genome Res.
867 2017;27(3):491–9.

868 76. Martin M. Cutadapt removes adapter sequences from high-throughput sequencing
869 reads. EMBnet J. 2011;17(1):10–2.

870 77. Kim D, Langmead B, Salzberg SL. HISAT: a fast spliced aligner with low memory
871 requirements. Nat Methods. 2015;12(4):357–60.

872 78. Liao Y, Smyth GK, Shi W. featureCounts: an efficient general purpose program for
873 assigning sequence reads to genomic features. Bioinformatics. 2014;30(7):923–30.

874 79. Love MI, Huber W, Anders S. Moderated estimation of fold change and dispersion for
875 RNA-seq data with DESeq2. Genome Biol. 2014;15(12):1–21.

876 80. Core R. TEAM, 2017. R: A language and environment for statistical computing. R
877 Foundation for Statistical Computing, Vienna, Austria. Online https//www r-project
878 org. 2022.

879 81. Szklarczyk D, Franceschini A, Wyder S, Forslund K, Heller D, Huerta-Cepas J, et al.
880 STRING v10: protein–protein interaction networks, integrated over the tree of life.
881 Nucleic Acids Res. 2015;43(D1):D447–52.

882

883

Figures 5 & 7

with

better resolution and contrast

Figure 5

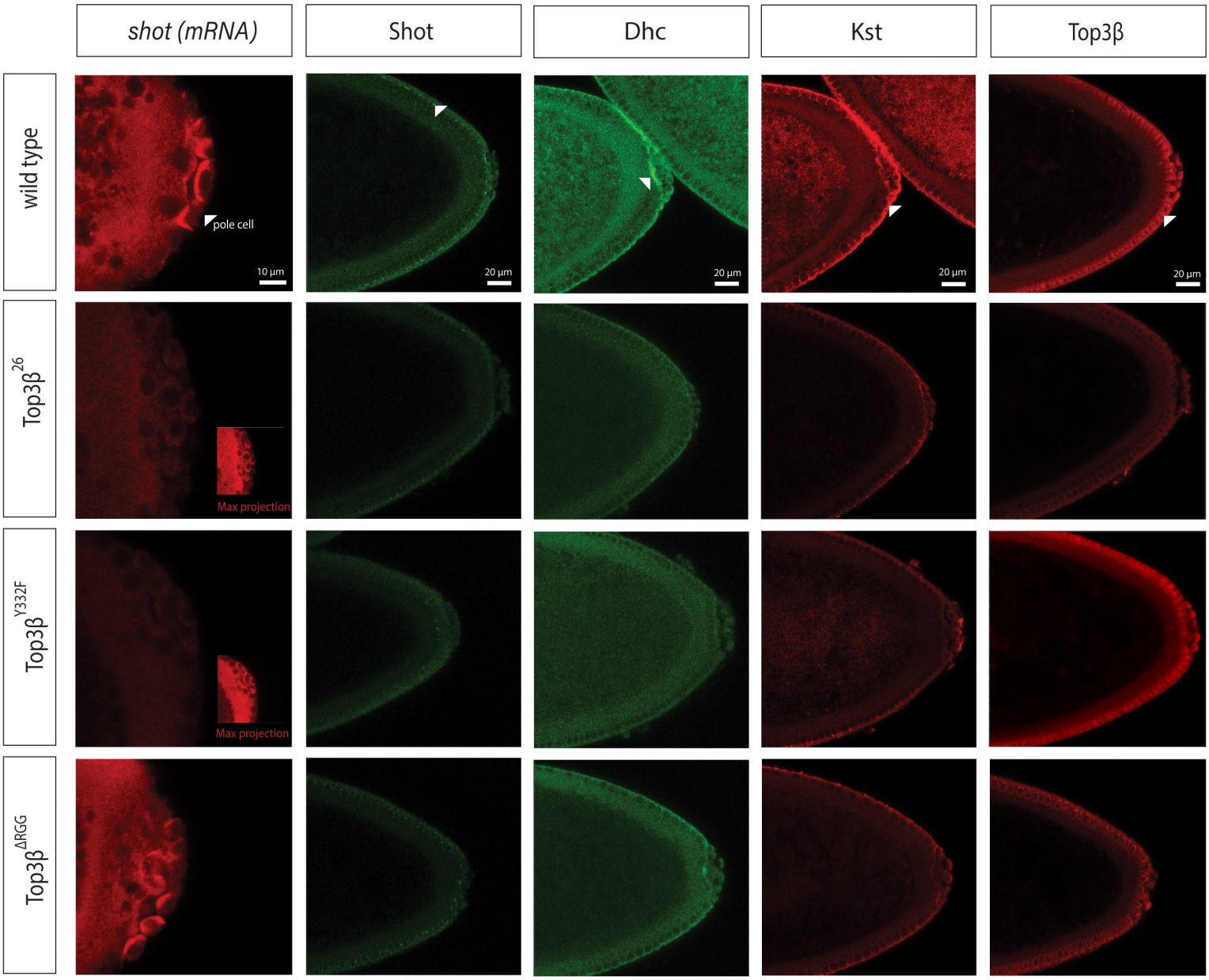
shot (mRNA)
Shot
Dhc
Kst
Top3β
wild type
Top3β26
Top3βY332F
Top3βΔRGG
pole cell
10 µm
20 µm
Max projection

Figure 7

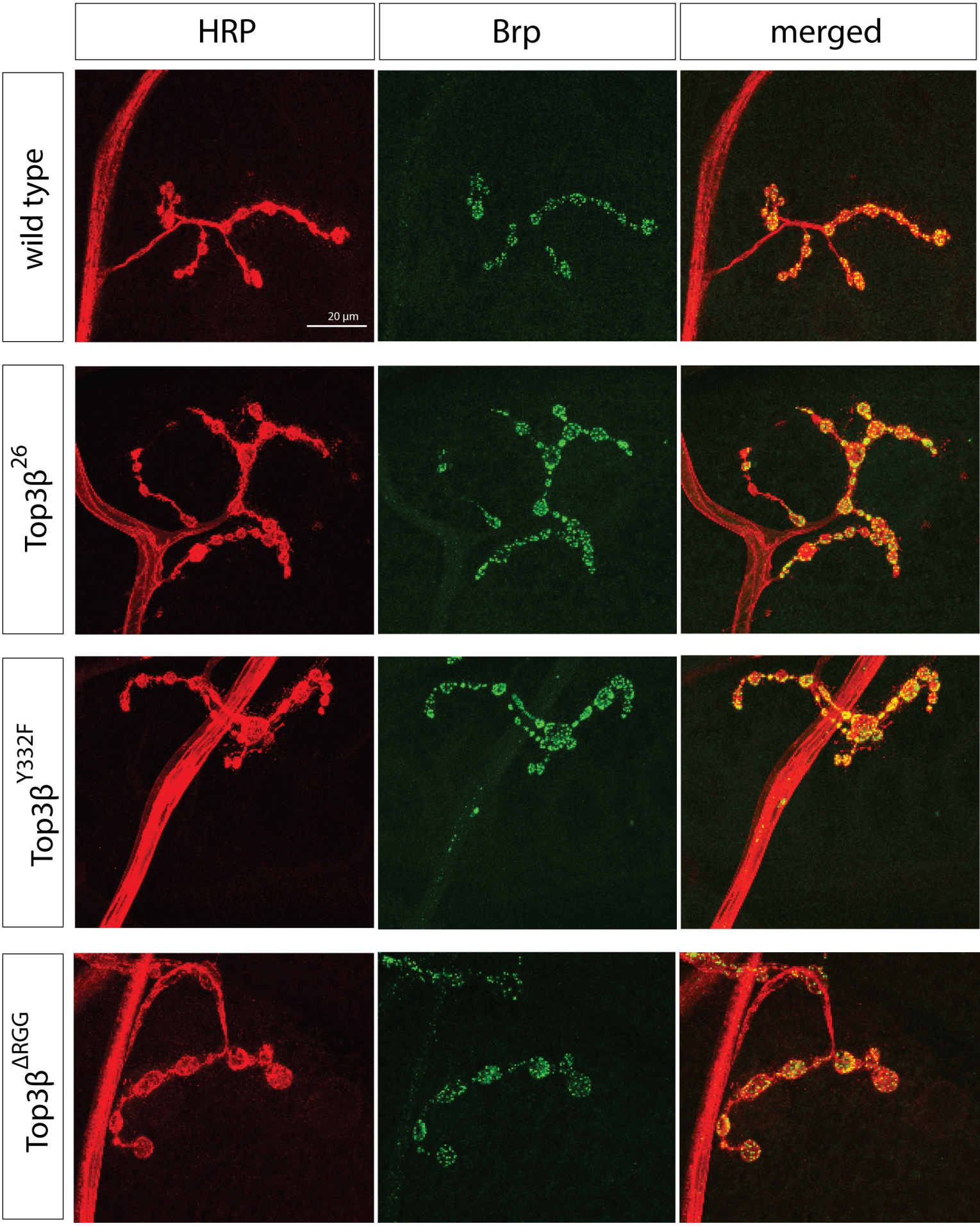
HRP
Brp
merged
wild type
Top3β26
Top3βY332F
Top3βΔRGG
20 µm